Jurassic magmatism and metamorphism in southern Colombia: regional correlations and tectonic implications

Marcela Restrepo Velásquez

Advisor:

Camilo Bustamante Londoño

School of Science
Earth sciences department
EAFIT University
Medellín
2019

Acknowledgments

This work was supported by the project *Magmatismo y metamorfismo Jurásico en Los Andes del Norte*.

I would like to express my deep and sincere gratitude to my advisor, Professor Camilo Bustamante, for his understanding, patience, continuous support, and his guidance all the time of research and writing of this work, but also, for giving me the chance to work with him, to share with me this and other projects, and for trust in me.

My sincere thanks also go to Professor Alejandro Beltrán, for the time he dedicated to teaching me the process of preparing samples for geochronological analysis, for performing the analyses on zircons, and for his help in interpreting the results.

I express my gratitude to Professor Agustin Cardona, for performing the geochronological analyses and fieldwork assistance; also, I thank Professor Andrés Bustamante, for his fieldwork assistance.

I thank my friends, Cristian Valencia, who also helped me and taught me how to prepare the samples for geochronological analyses; Luisa Fernanda Chavarría, for providing me the geochemical and geochronological information of Jurassic plutonic rocks of Colombia that she compiled and was used for this work; Daniel Monterrosa, for his help and advice to improve the geological maps presented in this work.

I am grateful to Elizabeth Romero, my dearest and closest friend, for being my support, for being there all the times I wanted to give up and always encouraged me to move on, for the sleepless nights we were working together before deadlines, and for all the fun we have had in the last five years.

Last but not least, I would like to thank my parents, José Gabriel and Maria Patricia, for their unconditional love, support, and sacrifices for educating and preparing me for my future.

Table of contents

List of figures

Page

List of tables

Page

Abstract

The Jurassic magmatic arc and the metamorphic belt of Colombia are the results of the interactions between the Farallon plate and the northwestern continental margin of South America. The former is constituted by an extense chain of batholiths that extends from the border with Ecuador to the Caribbean coast, and the latter is composed of rocks of intermediate pressure and temperature found along the Central Cordillera.

In southern Colombia, between Nariño and Putumayo region, were recognized a series of plutonic and metamorphic rocks not described until now in the geological maps. According to geochemical and geochronological analyses, the plutonic rocks found are granitoids that vary between granites, quartz monzonites, granodiorites, and diorites that presents a well-defined LILE and LREE enrichment and a well-defined Nb and Ti negative anomalies, characteristic of continental magmatic arcs, and crystallized during the Middle and Late Jurassic (ca. 174 -152 Ma), this age variation shows an apparent westward migration of the magmatism. On the other hand, metamorphic rocks correspond to hornblende-biotite schists metamorphosed under amphibolite facies conditions, which are in faulted contact with the granitoids, and record the crystallization age of its protolith, which corresponds to the Middle Jurassic (ca. 167 Ma).

Taken together, these new geochemical and geochronological data indicate the studied rocks are part of the Jurassic magmatic arc and metamorphic belt; also, the integration of these results with published information allows us to make some regional correlations to suggest that these rocks were formed due to an oblique convergence along the northwestern margin of South America.

1. Introduction

Subduction zones are tectonic expressions of convergent plate margins, where magmatism, metamorphism, and orogeny are complexly interrelated (Winter, 2014; Zheng and Chen, 2016). Subduction-related magmas are commonly characterized by its calc-alkaline character, contain significant amounts of volatiles (H_2O, CO_2), have a broad range of silica contents, and distinctive trace element patterns (e.g., enrichment in LILE relative to HFSE; negative Nb, Ti anomalies; Ducea et al., 2015). Regional metamorphism, in turn, is produced by the collision or accretion of continental or oceanic plates, producing rocks of medium to high temperatures and medium pressures (Feenstra and Franz, 2015). The interplay between magmatism and metamorphism at convergent margins can create the syntectonic emplacement of magmas (Paterson et al., 1989) or contact metamorphism at local scale (Bucher & Grapes, 2011). Identifying their temporality and tectonic relations is a fundamental task for reconstructing the tectono-magmatic and metamorphic history in subduction zones, such as the western margin of the Andes.

Since the Late Triassic and during the Jurassic, the northwestern margin of South America was affected by the subduction of the Farallon plate, and as a result of this process, a magmatic-arc belt was formed (Bayona et al., 2019). This magmatic arc is characterized by calc-alkaline magmas distributed longitudinally between the Central and Eastern Cordillera and extends latitudinally from the border with Ecuador to the Caribbean coast (Leal-Mejía et al., 2019). On the other hand, metamorphic rocks corresponding to this period are limited and have been related to Middle Jurassic collisional metamorphism produced by the accretion of para-autochthonous terranes with the NW margin of Colombia (Blanco-Quintero et al., 2014). New U-Pb ages in zircons from metamorphic rocks in other localities along the Andean margin of Colombia (Bustamante et al., 2017; Zapata-García et al., 2017) reveals that the Jurassic

metamorphic belt may have a regional extension, probably reaching the Cordillera Real in Ecuador (Bustamante et al., 2017).

Here we report new U-Pb ages in zircon along with whole-rock geochemistry from igneous and metamorphic rocks cropping out at the southwestern margin of Colombia, between the Nariño and Putumayo region. The main aim of this work is to: i) correlate this magmatism with the Jurassic magmatic belt of the Northern Andes, ii) identify the characteristics of the source and the processes that controlled the formation of these rocks and iii) determine crystallization and metamorphism ages on this magmatism and related metamorphic rocks. This allows us to establish the tectonic setting where these rocks were formed, and temporal relationships these magmatic rocks have with the metamorphic rocks they intrude, contributing to the discussion about the prolongation of the Jurassic metamorphic belt and its tectonic implications with the Jurassic magmatic arc of the Northern Andes.

2. Geological setting

In Colombia, the Andes branches into three major mountain ranges, the Western, Central, and Eastern Cordilleras, which are separated by the Cauca and Magdalena valleys.

The Western Cordillera comprises allochthonous oceanic sequences of basic volcanic rocks and Cretaceous marine sediments formed in a plateau tectonic setting that accreted to the continental margin since the Late Cretaceous (Villagómez et al., 2011; Quandt et al., 2018). The Central Cordillera consists of a Paleozoic-Early Mesozoic polymetamorphic basement intruded by an extensive Mesozoic-Cenozoic magmatic arc, which registered different collision and subduction events related to the agglutination of Pangea (Vinasco et al., 2006; Bustamante et al., 2010; Cochrane et al., 2014). Finally, the Eastern

Cordillera includes a Precambrian-Paleozoic metamorphic basement covered by Paleozoic-Upper Cretaceous marine and siliciclastic sedimentary sequences and intruded by Cretaceous gabbroic dikes and sills (Cortés et al., 2006; Mora et al., 2009; Vásquez et al., 2010).

During the Jurassic occurred the most extensive period of magmatic activity in Colombia due to the subduction of the Farallon plate along the northwestern margin of South America. This magmatic event is recorded in a discontinuous belt of batholiths distributed longitudinally between the Central and Eastern Cordillera and extends latitudinally from the border with Ecuador to the Caribbean coast (Aspden et al., 1987; Leal-Mejía et al., 2019 Bayona et al., 2019; Fig.1). Aspden et al., (1987) defined two events of greater magmatic activity: the first event occurs between 210 ± 7 and 192 ± 7 Ma and the second, which identifies as the main event, between 183 ± 5 to 142 ± 6 Ma. This magmatism is associated with extrusive rocks that show an explosive and effusive character, which proposes that these rocks were located at shallow levels and had a prolonged tectono-magmatic evolution (Bustamante et al., 2010).

Different models have been proposed to explain the evolution of this magmatism. The first model establishes that the magmatism underwent trenchward migration due to slab roll-back, which causes back-arc extension, crustal thinning, and isotopically juvenile magmas (Cochrane et al., 2014; Spikings et al., 2015). The second model proposes an eastward migration away from the trench as a result of subduction erosion of the accretionary prism, where the subducted sediments allow the increase of the water flux and decrease the solidus temperature, thus, the magma production increase (Rodríguez et al., 2018; García, 2018). Finally, the third model postulates the formation of a stationary arc due to oblique convergence of the Farallon plate; this process caused a long-term evolution of the magma sources and a decrease in magmatic fertility with time (Bustamante et al., 2016).

On the other hand, Jurassic metamorphism is less extense than the Jurassic magmatism; therefore, its record is limited (Fig. 1). Nevertheless, metamorphic rocks of this period have been reported in geological units and regions such as the San Lorenzo schists, located in the Santa Marta Massif (Piraquive, 2016), the Santander Massif (Zuluaga et al., 2017), along the Central Cordillera in the Tierradentro gneisses and amphibolites unit and the Cajamarca Complex (Bustamante et al., 2017; Blanco-Quintero et al., 2014; Rodríguez et al., 2018), the Garzón Massif and the Colombian Massif in the La Cocha-Río Téllez Migmatitic Complex (Jiménez-Mejía, 2003; Zapata-García et al., 2017).

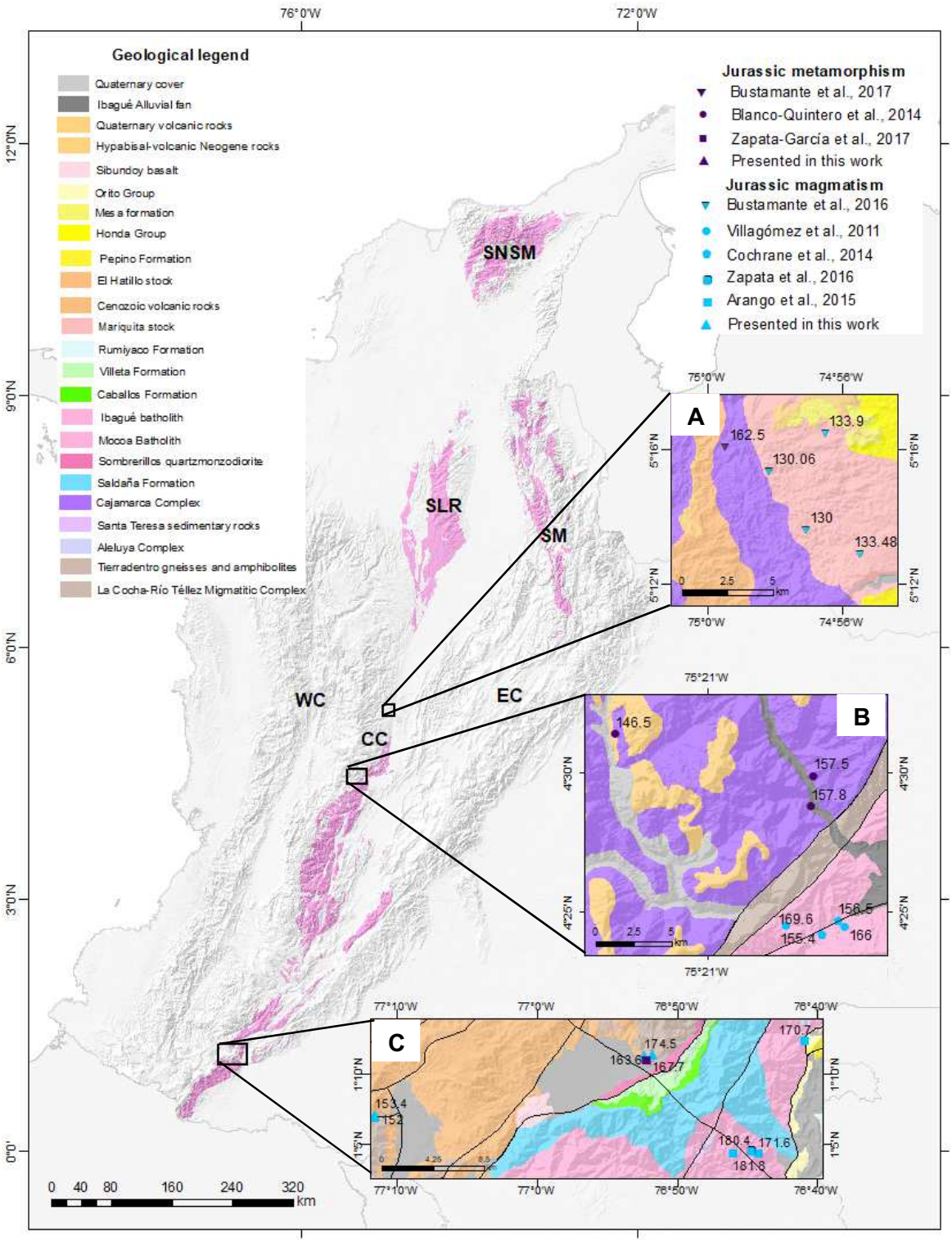

Figure 1. Jurassic magmatic rocks and Jurassic metamorphic rocks from the Colombian Andes. **SNSM**: Sierra Nevada de Santa Marta; **SLR**: San Lucas Range; **SM**: Santander Massif; **WC**: Western Cordillera; **CC**: Central Cordillera**; EC:** Eastern Cordillera. **A.** North of Tolima region **B.** Central Cordillera, between the towns of Ibague and Cajamarca and along the Combeima River. **C.** Southern Colombia, between Nariño and Putumayo region.

2.1. Magmatism and metamorphism between Nariño and Putumayo region

In the study area outcrops metamorphic rocks as La Cocha-Río Téllez Migmatitic Complex, and two large plutonic bodies, which are Mocoa Batholith and Sombrerillos quartz monzodiorite (Fig. 2).

The La Cocha-Río Téllez Migmatitic Complex includes migmatites, schists, gneisses, and amphibolites. It is in faulted contact with the Sombrerillos quartz monzodiorite and with Cretaceous sedimentary rocks and intruded by the Mocoa Batholith. Additionally, this is covered by the Saldaña Formation and partially covered by Quaternary lavas and pyroclasts. Núñez (2003) suggests a Precambrian age for this complex based on the stratigraphic observations. However, Jiménez-Mejía (2003) and Zapata-García et al., (2017) reported a U-Pb zircon age of 166 ± 4 Ma and 163.6 ± 4.7 Ma, in the region of Garzón and the municipality of San Francisco respectively.

The Sombrerillos quartz monzodiorite varies between quartz monzonite, granodiorite, granite, monzogranite, and gabbronorite. It is in faulted contact with Paleozoic lodolites and limestones, and with the Saldaña Formation (Núñez, 2003). There is no geochronological data available of this plutonic body in the study area; however, García (2018) reported a U-Pb zircon age of 189 ± 7 Ma in the region of Garzón (the Eastern Cordillera).

The Mocoa Batholith is composed of monzogranites, granodiorites, quartz monzonites, and granites; also, porphyric facies can be observed towards the edges of the body. This batholith is in faulted contact with Cretaceous-Paleogene sediments of the Caballos, Villeta, Rumiyaco, and Pepino Formations, and intrude the La Cocha-Río Téllez Migmatitic Complex and the Saldaña Formation (Núñez, 2003; Arango et al., 2015); Its stratigraphic

relationship with the Sombrerillos quartz monzodiorite is not clear (García, 2018). According to U-Pb zircon analyses, this plutonic body yields a crystallization age ranging between 181.8 ± 1.3 Ma to 170.7 ± 2.1 Ma (Arango et al., 2015).

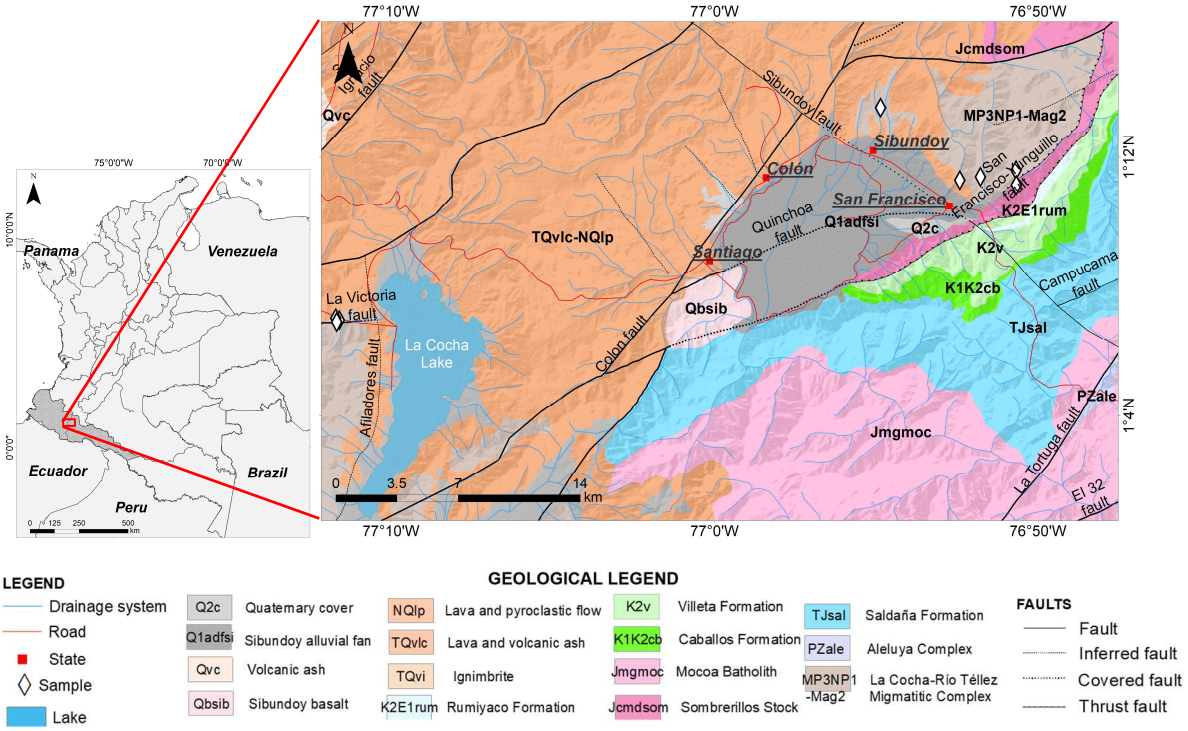

Figure 2. Localization and geological map of the studied area, including sample location. Modified from Núñez (2003).

3. Methods

3.1. Survey planning and fieldwork

According to bibliographic review carried out, three areas of interest were chosen for the recognition and collection of samples, these areas correspond to the north of the municipality of Sibundoy, to the northeast of the municipality of San Francisco, which are grouped into what it is known as the Sibundoy Valley (Putumayo region), and to the west of the Laguna de la Cocha, on vereda El Motilón (Nariño region).

During the fieldwork were collected samples of igneous and metamorphic rocks in order to describe their texture, grain size, and mineralogical composition. In addition, structural features, where possible, were measured including orientations, foliation planes, and structures like dikes.

3.2. Petrographic analyses

Thin sections were prepared in order to recognized mineralogy, degree of alteration, and microstructures; microscopic descriptions were made using a petrographic microscope, and photomicrographs were taken with a digital microscope camera (Moticam 580), all process was performed in the Mineralogy and petrology Laboratory of EAFIT University.

3.3. Whole-rock geochemistry

Mayor oxides and trace elements concentrations were determined for thirteen samples by x-ray fluorescence (XRF) and inductively coupled plasma-mass spectrometry (ICP-MS) at ALS Minerals. The samples were crushed using a jaw crusher and powered using a tungsten carbide ring mill. The powered samples (0.2 g) are weighted into a graphite crucible and mixed with 1.5 g of $LiBO_2$ flux. The crucibles are heated in a furnace to 1050°C for 15 minutes, and the resulting melt is dissolved in 5% HNO_3. Calibration standards and reagent blanks are added to the sample sequence. Sample solutions are aspirated into an ICP emission spectrograph (Jarrel Ash Atom Comb 975) for determining major oxides and certain trace elements (Ba, Nb, Ni, Sr, Sc, Y and Zr), while the sample solutions are aspirated into an ICP-MS (Perkin-Elmer Elan 6000) in order to determine trace elements, including rare earth elements.

All geochemical analyses were handled and processed using the software GCDKit, 5.0 (Janoušek et al., 2006)

3.4. Zircon U–Pb Geochronology

Zircon separation followed standard procedures (e.g., Mange and Maurer 1992) and was performed at EAFIT University facilities. Rock samples were crushed with a conventional jawbreaker, and the heavy mineral fraction was separated from the 400-63 microns fraction by using a pan. Hand-picking of zircon grains from the heavy mineral concentrates was randomly performed in each sample. After mounting in the epoxy-pill, zircon grains were polished and carbon-coated at ETH Zurich facilities. Zircon cathodoluminescence (CL) imagery was carried out to evaluate the magmatic zonation, metamorphic origin, rims, and inherited cores. For this purpose, we used a JEOL JSM-6390LA scanning electron microscope (SEM) at the Institute for Geochemistry and Petrology at ETH Zurich. Zircon U–Pb geochronology was performed through laser ablation inductively coupled mass spectrometry (LA-ICP-MS) at ETH Zurich, and laser ablation spots (19 microns) were selected in both cores and rims when it was possible.

3.4.1. LAICPMS Analytical parameters and specifications

In situ U-Pb geochronology were conducted by laser ablation inductively coupled plasma mass spectrometry (LA-ICP-MS) at the Institute of Geochemistry and Petrology, ETH Zurich using a 193 nm Resolution (S155) ArF excimer laser coupled to an Element SF ICPMS (Guillong et al., 2014; von Quadt et al., 2016). The output energy was typically ca. 2 J/cm^2 and a 5 Hz pulse repetition rate was used. The ablation was under helium flow of 0.7 L/min. Argon was admixed to the aerosol within the funnel of the ablation cell to transport the ablated

material to the ICP for ionization. Dwell times range from 5 – 30 ms and peak hopping was employed. Oxide generation was optimized at ThO^+/Th^+=<0.3%. For each analysis a baseline was measured for 30 seconds followed by 30 seconds of ablation. Elemental concentrations were calculated using the IGOR based Iolite software (Paton et al., 2011). The stoichiometric Si concentration of 15.2 wt.% for zircon was used as an internal standard. SRM NIST 612 glass (Hinton, 1999) was used as the primary external trace element standard and was measured four times each 25 zircon analyses.

The masses 202, 204, 206, 207, 208, 232, 235, and 238 were measured. Total ablation time was set to 30 seconds with a gas blank/background measurement of 10s. Age data were collected in runs of 20 samples bracketed before and after by two analyses of the primary reference material GJ-1 (Jackson et al., 2004) and each one of secondary reference zircons 91500 (Wiedenbeck et al., 1995), Temora (Black et al., 2003; von Quadt et al., 2016), Plesovice (Slama et al., 2008), AusZ7.5 (von Quadt et al., 2016) and SA2 (von Quadt, not published, personal communication). Data reduction was performed with the IGOR based Iolite v2.5 (Paton et al., 2011) and Vizual Age (Petrus and Kamber, 2012) software.

Statistical analyses of zircon data were performed using Isoplot 4.15 (Ludwig, 2012). Only zircons with concordance higher than 90% were accepted and plotted.

4. Results

4.1. Fieldwork relationships and petrography

4.1.1. Plutonic rocks

Eight samples were collected in two localities, which are the San Francisco River (JC001, JC002) and in the northeast of the municipality of San Francisco (JC003A, JC004, JC009, JC010, JC011, JC012; Fig. 3). The outcrops of the rocks were found mostly along tiny waterfalls; sample JC003A was found in faulted contact with metamorphic rocks (sample JC003B; see section 4.1.2), and samples JC010 and JC012 are dikes intruding samples JC009 and JC011 respectively. These dikes present an NW trending and dip to the east.

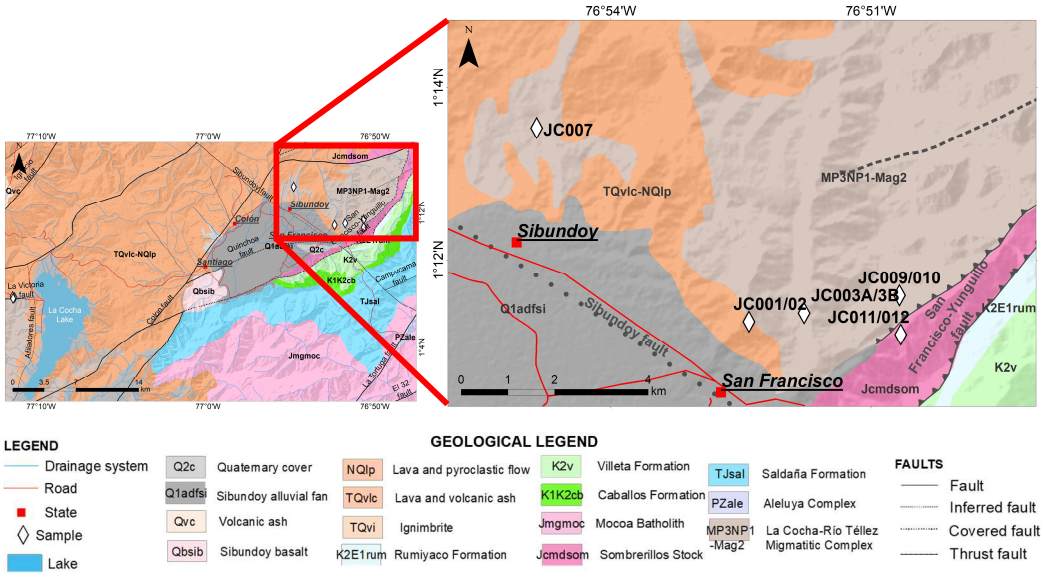

Figure 3. Geological map of the study area. The inset shows samples location in the Sibundoy Valley

Hand specimens present phaneritic texture, felsic to intermediate composition, equigranular crystal size that varies between fine and medium (0.2-5 mm), and are mainly composed of quartz, feldspar, biotite, and hornblende.

Thin sections of samples JC001 and JC002 (Fig. 4 A, B) shows that are fine-grained rocks, holocrystalline, allotriomorphic, display a phaneritic texture and composed of quartz (40-45%), plagioclase An_{4-45} (25-30%), potassium feldspar (10-15%), biotite (10-12%), and muscovite (4%). Accessory minerals include opaque minerals, apatite, and zircon.

Sericite and epidote are found as secondary minerals replacing plagioclase. These samples were classified as granites.

Quartz crystals have fine-sized anhedral crystals between 0.2 and 1.2 mm, and present chess-board pattern, and undulose extinction; **plagioclase** forms fine-sized subhedral crystals that range from 0.5 to 1.2 mm, and some crystals are zoned; **potassium feldspar** occur as fine-sized subhedral crystals (0.5-1.1 mm); **biotite** presents fine-sized subhedral crystals (0.5-1 mm); **muscovite** forms fine-sized anhedral crystals of 0.2 mm; **opaque minerals** occur as fine-sized anhedral crystals that range from 0.2 to 0.5 mm; **apatite** presents subhedral-euhedral crystals less than 0.2 mm; and **zircon** forms subhedral crystals less than 0.1 mm.

Sample JC003A (Fig. 4C) presents a phaneritic texture, is a medium-grained rock, holocrystalline, hypidiomorphic, constituted by plagioclase An_{35} (30%), microcline (15%), quartz (10%), biotite (25%), and hornblende (15%). Sphene, apatite, zircon, and opaque minerals are accessory minerals. Sericite, clay, and epidote are secondary minerals replacing plagioclase, and chlorite is replacing biotite. Microstructures such as myrmekites, microcline twinning, undulose extinction in quartz, and poikilitic texture (hornblende as oikocryst and plagioclase as chadacrysts) were found. The sample was classified as quartz monzonite.

Plagioclase occurs as medium-sized subhedral-euhedral crystals that vary from 1.2 to 3 mm, some of the crystals are fractured (3%) and zoned, **microcline** presents medium subhedral-anhedral crystals of 2-2.8 mm, **quartz** forms fine to- medium-sized anhedral crystals between 0.7 and 1.6 mm, **biotite** presents subhedral crystals that range between 0.5 and 1.5 mm, **hornblende** occur as medium-sized

subhedral crystals (1-1.5 mm), **sphene** presents subhedral crystals less than <0.3 mm, **apatite** forms euhedral crystals less than 0.1 mm, **zircon** occurs as subhedral-euhedral crystals less than 0.1 mm and **opaque minerals** form subhedral crystals less than 0.2 mm.

Samples JC004 and JC011 (Fig. 4D, E) varies from fine to medium-grained rocks, they are holocrystalline, hypidiomorphic, displays a phaneritic texture and composed of quartz (10-30%), plagioclase (15-20%), microcline (10-35%), biotite (20%), hornblende (10-15%). Accessory minerals include opaque minerals, sphene, epidote (JC004), and apatite (JC011). Secondary minerals such as sericite and clay are found replacing plagioclase. Undulose extinction, microcline twinning, and myrmekites are microstructures included in the sample. They were classified as granodiorites.

Quartz forms fine to- medium-sized anhedral crystals (0.8-2 mm), **plagioclase** presents fine to- medium-sized subhedral crystals that range from 0.4 to 1.5 mm, most of them are zoned and presents deformation twins, **microcline** occurs as anhedral crystals that range from less than 0.2 mm to 1.5 mm, **biotite** presents fine to- medium-sized subhedral indicates (0.6-2 mm), some crystals are deformed (10% -sample JC011), **hornblende** forms subhedral crystals that range from 0.5 to 1.1 mm, **opaque minerals** occur as subhedral-anhedral crystals that range from less than 0.25 mm to 1.1 mm, **sphene** forms fine-sized subhedral crystals (0.3 and 0.7 mm), **epidote** presents fine-sized subhedral crystals (0.2 and 0.6 mm), and **apatite** forms very fine-sized euhedral crystals less than 0.1 mm.

Sample JC009 (Fig. 4F) presents a phaneritic texture, is a medium-grained rock, holocrystalline, hypidiomorphic, constituted by plagioclase (50%), microcline (10%), quartz (5%), biotite (20%), hornblende (10%).

Accessory minerals include opaque minerals and epidote, and secondary minerals such as sericite and clay are found replacing plagioclase. Microstructures such as myrmekites, microcline twinning, and undulose extinction in quartz were found. This sample was classified as diorite.

Plagioclase occurs as medium-sized subhedral-euhedral crystals (1-1.5 mm), some twins are slightly deformed, **microcline** forms fine-sized subhedral crystals that range from 0.2 to 1 mm, **quartz** presents fine-sized anhedral crystals (0.4-1 mm), **biotite** forms medium-sized subhedral crystals (0.7-2 mm), **hornblende** occur as medium-sized subhedral crystals that range between 1.1 and 1.5 mm, **opaque minerals** have very fine-sized anhedral crystals less than 0.25 mm, and **epidote** forms fine-sized subhedral crystals of 0.2 mm.

Samples JC010 and JC012 (Fig. 4G, H) present phaneritic texture and noticeable differences in crystal size, the sample JC010 display fine-sized and equigranular crystals (<0.7 mm), while the sample JC012 present medium-sized and inequigranular crystals, they are holocrystalline and hypidiomorphic, composed of plagioclase An_{56} (13-40%), hornblende (50-80%) and biotite (5%); the sample JC010 is constituted by accessory minerals such as opaque minerals, sphene, and apatite; secondary minerals such as sericite, clay, and calcite are found replacing plagioclase, and chlorite replacing hornblende. These samples were classified as hornblende gabbros.

Plagioclase forms fine-sized subhedral crystals that range between <0.25 and 0.5 mm, some crystals are zoned, **hornblende** presents medium-sized subhedral crystals (0.6 and 1.1 mm), **biotite** occur as fine-sized subhedral crystals (0.3 and 0.4 mm), **opaque minerals** have very fine-sized subhedral-euhedral crystals (<0.25 mm), **sphene**

presents fine-sized subhedral crystals of 0.2 mm, and **apatite** forms very fine-sized euhedral crystals less than 0.1 mm. Both samples exhibit a polygonal texture.

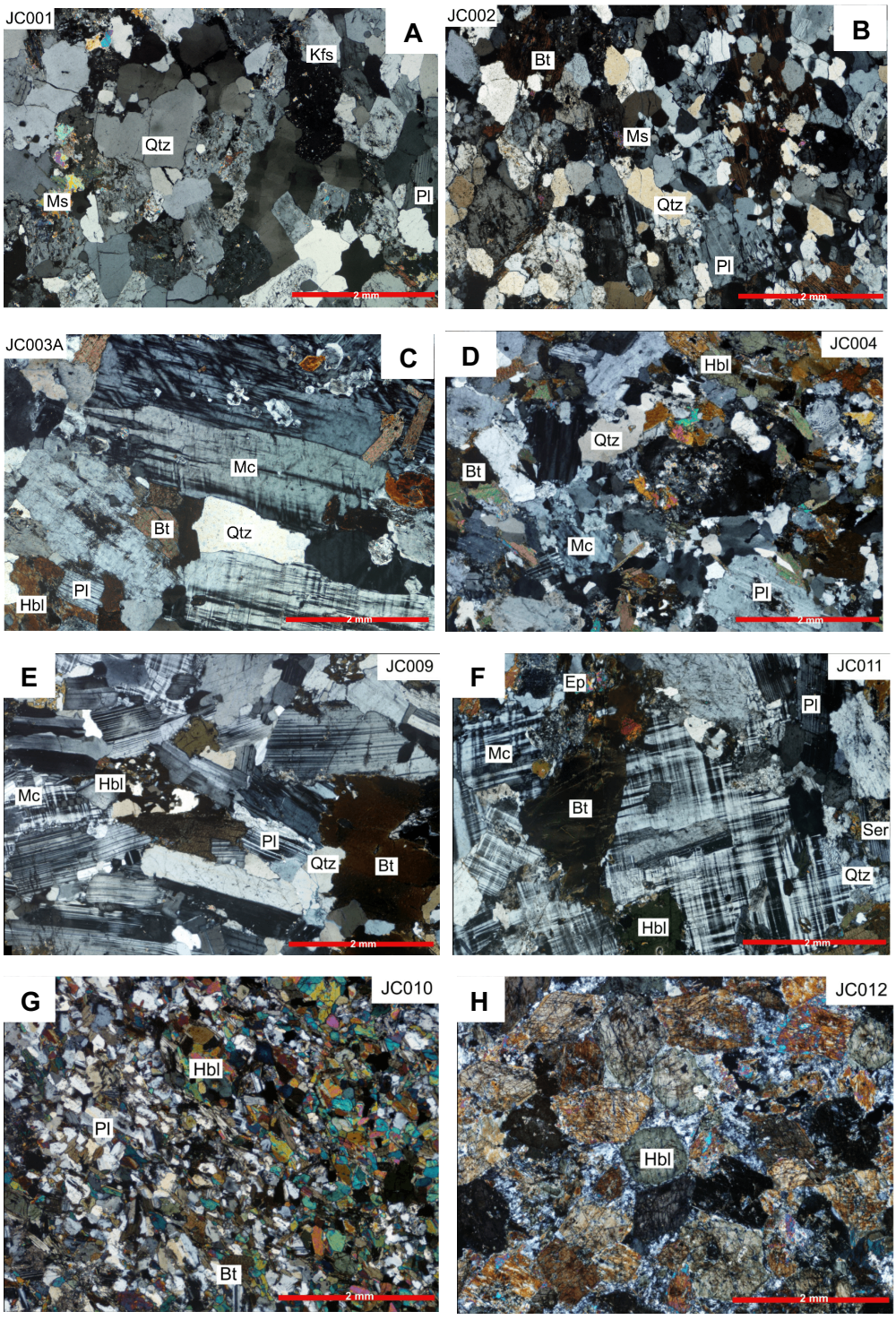

Figure 4 Photomicrographs of plutonic samples from the Sibundoy Valley in crossed polarizers. A. Sample JC001 B. Sample JC002 C. Sample JC003A D. Sample JC004

E. Sample JC009 F. Sample JC011 G. Sample JC010, H. Sample JC012; Qtz = Quartz, Kfs = Potassium feldspar, Bt= Biotite, Ser= Sericite. Pl= Plagioclase, Bt= Biotite, Hbl= Hornblende, Mc= Microcline.

Three plutonic samples were collected in vereda El motilón at the western margin of La Cocha lake (JC014A, JC015, JC016; Fig.5). Sample JC014A present mylonitic foliation with a NE trend and dip to the SE (N40E/26°SE).

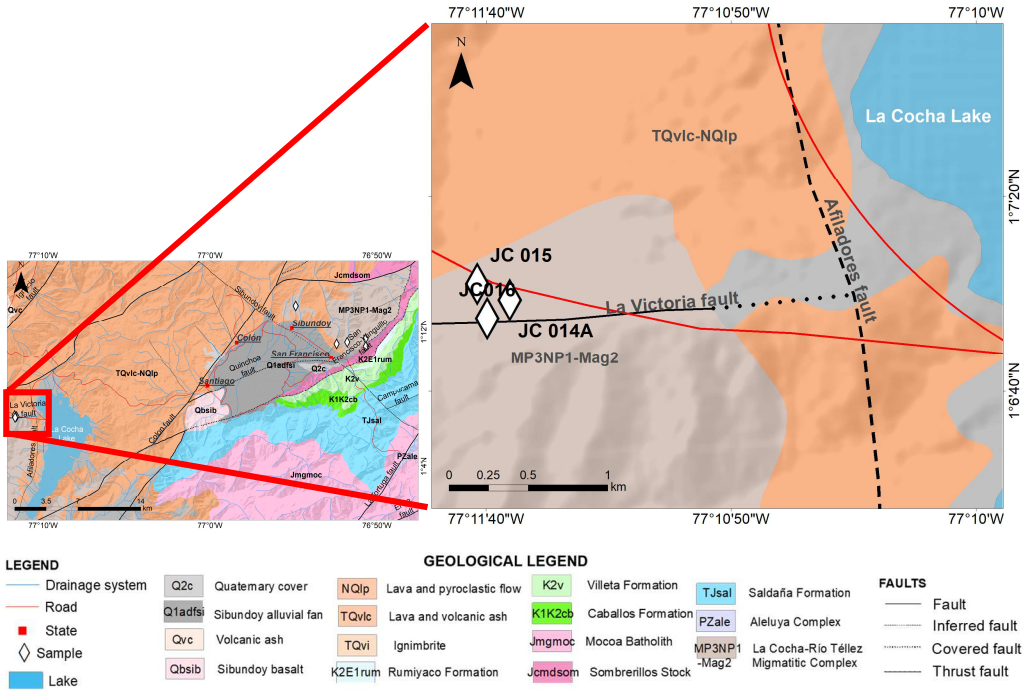

Figure 5. Geological map of the study area. The inset shows samples location in La Cocha Lake

Hand specimens present phaneritic texture, felsic composition, medium-sized inequigranular crystals, and are mainly composed of quartz, feldspar, and biotite.

Sample JC014A (Fig. 6A) present medium-sized inequigranular crystals, display a phaneritic texture, is holocrystalline, allotriomorphic, and deformed; constituted by quartz (40%), plagioclase (25%), biotite (15%), hornblende (15%), accessories minerals such as epidote, and secondary minerals like sericite and clay replacing plagioclase, and chlorite replacing biotite. This sample was classified as diorite.

Quartz has fine-sized anhedral crystals that range from 0.2 to 0.7 mm, **plagioclase** forms fine-sized subhedral-anhedral crystals (0.3-0.8 mm), **biotite** occur as fine-sized subhedral crystals (0.2-0.6 mm), **hornblende** presents medium-sized anhedral crystals that range between 0.3 and 1.1 mm, some gems are altered to biotite (30%), and **epidote** forms very fine-sized anhedral crystals less than 0.5 mm, is disseminated throughout thin section.

Samples JC015 and JC016 (Fig. 6B, C), present medium-sized inequigranular crystals, display a phaneritic texture, is holocrystalline, allotriomorphic, weathered and deformed; composed of quartz (40-45%), plagioclase (35-50%), potassium feldspar (10%), biotite (3-9%), hornblende (1%), accessories minerals include epidote, opaque minerals, zircon, and apatite. Sericite and clay are found replacing plagioclase and chlorite replacing biotite. Microstructures found are consertal, undulose extinction, and quartz recrystallization. They were classified as granites.

Quartz has medium-sized anhedral crystals (1.1-2.5 mm), some crystals are fractured, **plagioclase** forms fine-sized subhedral crystals that range from 0.4 to 1.1 mm, in the case of the JC015 sample, slightly deformed cores are observed, **biotite** presents fine-sized anhedral crystals (0.3-0.7mm), **hornblende** occur as fine-sized euhedral crystals of 0.7 mm, **epidote** forms fine-sized anhedral crystals that range between 0.3 and 0.5 mm, **opaque minerals** forms very fine-sized anhedral crystals less than 0.25 mm, **zircon** very fine-sized euhedral crystals less than 0.1 mm, and **apatite** forms subhedral very fine-sized crystals (<0.1 mm).

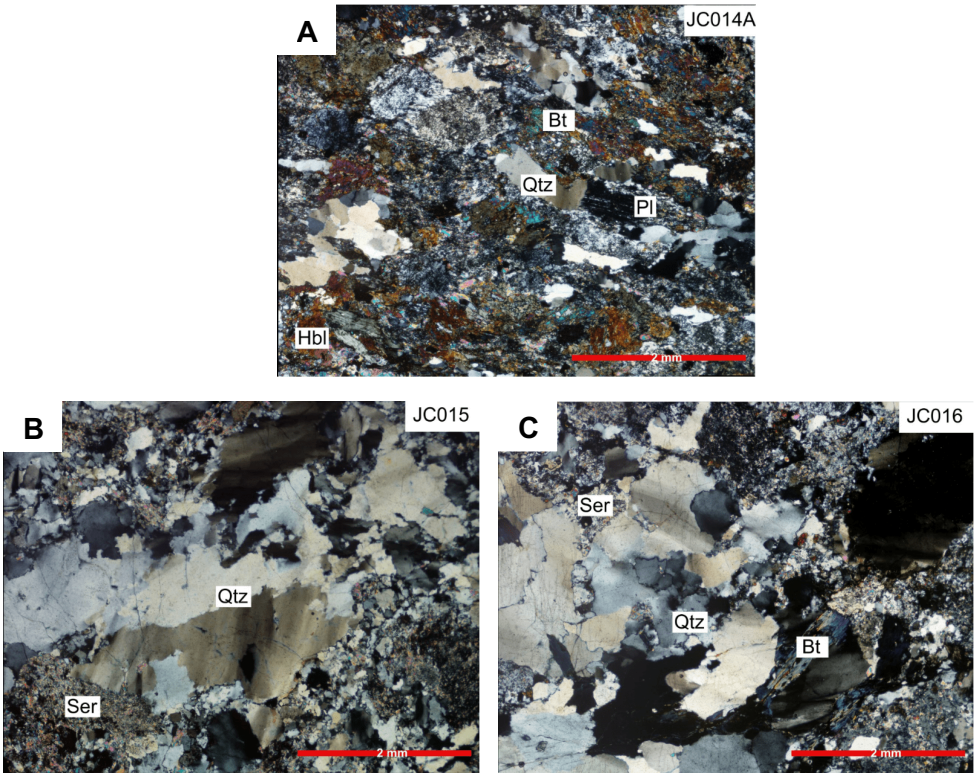

Figure 6 Photomicrographs of samples from La Cocha Lake in crossed polarizers. A. Sample JC014A. B. Sample JC015. C. Sample JC016; Qtz= Quartz, Bt= Biotite, Ser= Sericite. Pl= Plagioclase, Bt= Biotite, Hbl= Hornblende.

4.1.2. Metamorphic rocks

Two metamorphic samples were collected in two localities: at the northeast of San Francisco (JC003B), and to the north of Sibundoy, on the La Hidráulica river (JC007; see figure 3). As aforementioned, sample JC003A is in faulted contact with sample JC003B (Fig. 7). Hand specimens of these samples are black quartz-biotite schists with quartz veins less than 2 mm (sample JC003B).

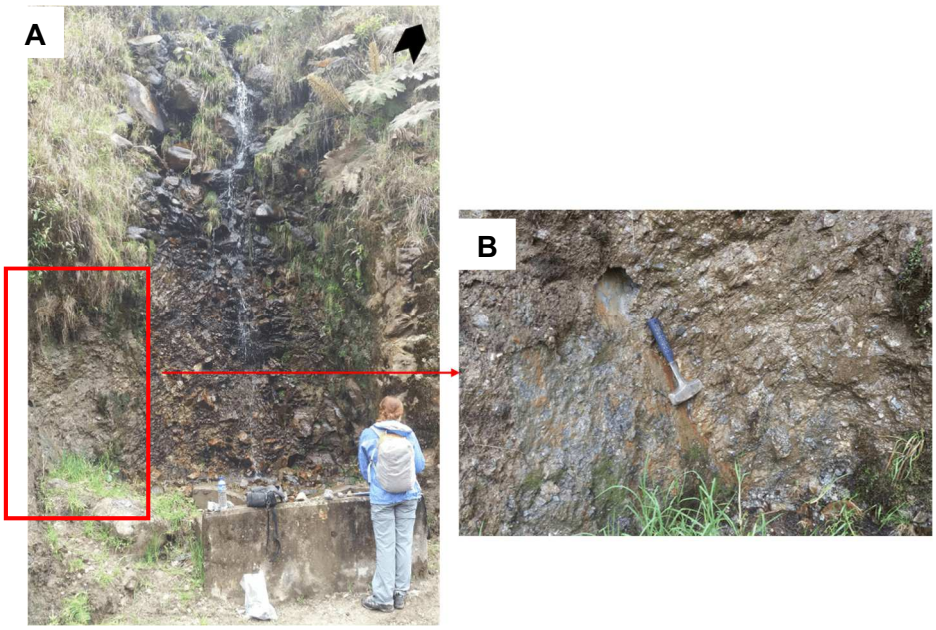

Figure 7. A. Samples JC003B and JC003A outcrop at the northeast of San Francisco. **B.** Faulted contact between sample JC003B (left) and sample JC003A (right).

Thin sections (Fig. 8A, B) shows that the samples are fine- to medium-size grained schist with grano-lepidoblastic texture, and are composed of biotite (30-40%), plagioclase An_{31-36} (10%-20%), quartz (15%-35%), hornblende (15-30%), and opaque minerals, apatite, zircon, and epidote as accessory phase. Biotite and hornblende define the main foliation.

Biotite forms fine- to medium-sized subidioblastic grains that vary from less than 0.25 mm to 2 mm, **plagioclase** presents very fine- to fine-sized xenoblastic grains (<0.25-0.4 mm), **quartz** occurs as very fine-sized xenoblastic grains (<0.2 y 0.8 mm) with undulose extinction, **hornblende** presents fine-sized grains xenoblastic that range from 0.2 mm to 0.5 mm, **opaque minerals** have very fine-sized xenoblastic grains less than 0.2 mm, **apatite** forms very fine-sized idioblastic grains (<0.1 mm), **zircon** have very fine-sized subidioblastic-idioblastic grains less than 0.1 mm, and **epidote** occurs as fine-sized xenoblastic grains of 0.3 mm.

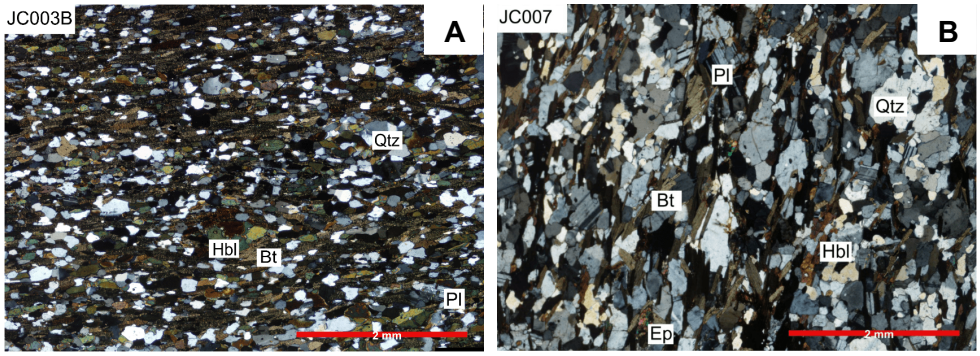

Figure 8. Photomicrographs of metamorphic samples of the Sibundoy Valley in crossed polarizers. **A**. Sample JC003B **B**. sample JC007; Qtz= Quartz, Pl= Plagioclase, Bt= Biotite, Hbl= Hornblende, Ms= Moscovite, Ep= Epidote.

4.2. Whole-rock geochemistry

Major oxide and trace elements data were acquired from thirteen samples, in which eleven samples are from the Sibundoy Valley and La Cocha Lake and two metamorphic samples from the Sibundoy Valley. Geochemical results are presented in Table 1 (see appendix). Additionally, we integrate published results with the newly obtained data from several localities of the Jurassic magmatic arc, in order to compare and establish if they share similar geochemical trends.

4.2.1. Plutonic rocks

Samples have SiO_2 contents from 43.3 to 75.0 wt.%, Al_2O_3 values range between 12.1 and 18.5 wt. %, Na_2O from 2.6 to 5.1 wt% and CaO, MgO, and K_2O show a wide range of values, ranging from 1.4 to 9.9 wt.%, from 0.5 to 11.9 wt.% and from 0.9 to 3.4 wt.% respectively. Mg# values range from 21.2 to 55.5. The loss on ignition (LOI) for most of the analyzed samples is less than or equal to 2.0 wt%, with two samples yielding values of 2.8 and 5.4 wt% that reflect an intermediate-high degree of alteration (samples JC010 and JC012). Bivariate

diagrams show a decrease in TiO_2, $Al2O_3$, MgO, CaO, P_2O_5, and Fe_2O_3, and a subtle increase in Na_2O and K_2O relative to SiO_2 (Fig. 9).

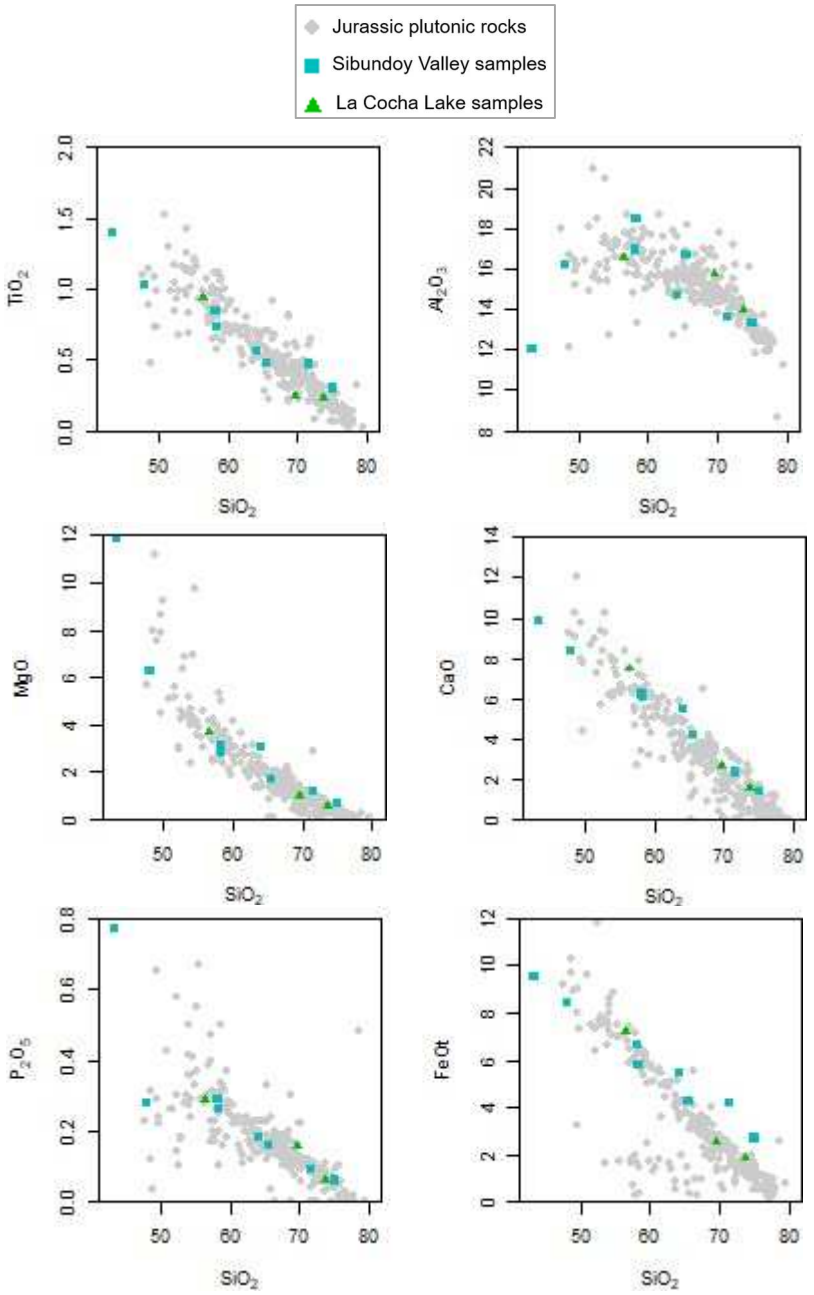

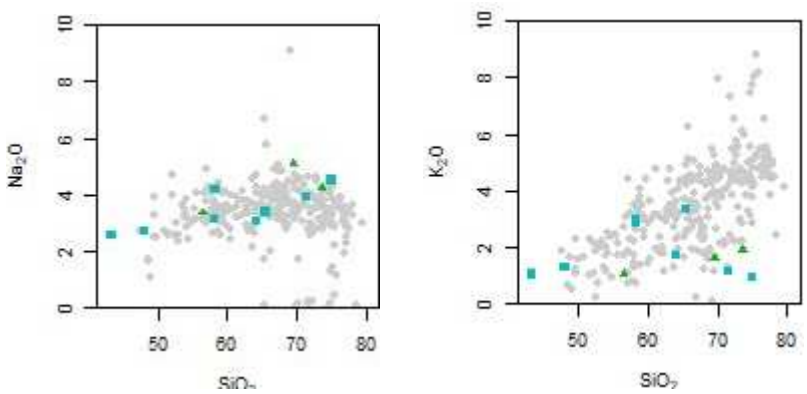

Figure 9. Bivariate diagrams of plutonic igneous samples from the Sibundoy Valley and La Cocha Lake.

A clear differentiation trend from basic to acid composition is seen in the total alkalis vs. silica (TAS) diagram (Fig 10A). The alumina saturation index ranges from metaluminous (seven samples) to peraluminous (four samples; Fig. 10B), this peraluminous trend is due to mineralogical composition (presence of biotite and muscovite), high SiO_2 contents (higher than 65 wt%), the alteration degree and LOI values of samples JC001, JC002, JC015, and JC016. Most of the samples plots in the calc-alkaline field and only two in the tholeiite field according to the alkalinity index diagram of Peccerillo and Taylor (1976) (Fig. 10C).

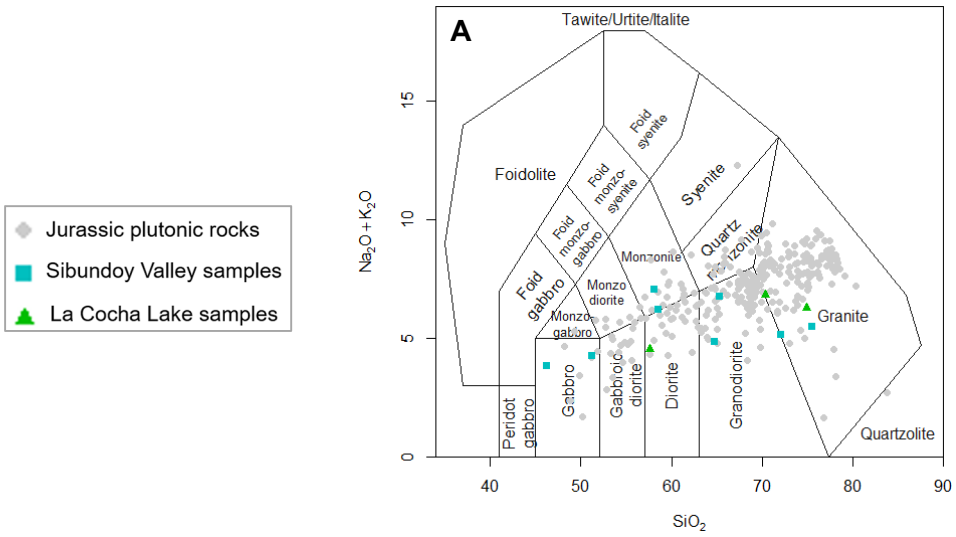

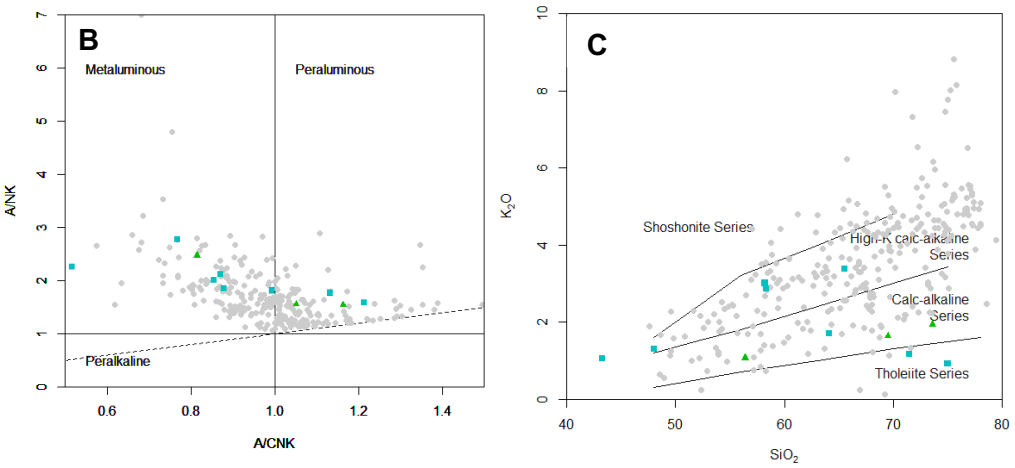

Figure 10. Geochemical classification and discrimination diagrams of plutonic igneous samples from the Sibundoy Valley and La Cocha Lake. A: Classification of plutonic rocks based on the TAS diagram of Middlemost (1994). B: Alumina saturation index diagram of Shand (1943) **C:** Alkalinity index diagram of Peccerillo and Taylor (1976).

Multi-element diagram normalized to the primitive mantle (Sun & McDonough, 1989; Fig. 11) shows negative anomalies of Nb and Ti, depletion of HFSE, and positive anomalies of Pb, K, Ba.

According to the REE diagram normalized to chondrite (Nakamura, 1974; Fig. 12) The rocks have steep REE patterns ((La/Yb)N = 2.5 - 30.4), show an enrichment in LREE compared with HREE ((La/Sm)N= 2.3-6.4, (Tb/Yb)N= 0.9-2.5), the LREE-MREE slope is steep negative ((La/Dy)N= 3.0-16.5), and the MREE-HREE slope is flat-shaped ((Dy/Yb)N= 0.5-1.2). Eu anomaly is negative; only sample JC016 has a positive anomaly (Eu/Eu*= 0.6-1.1). According to the tectonic discrimination diagram of Harris et al., (1986), the samples plot in the volcanic arc field (Fig. 13).

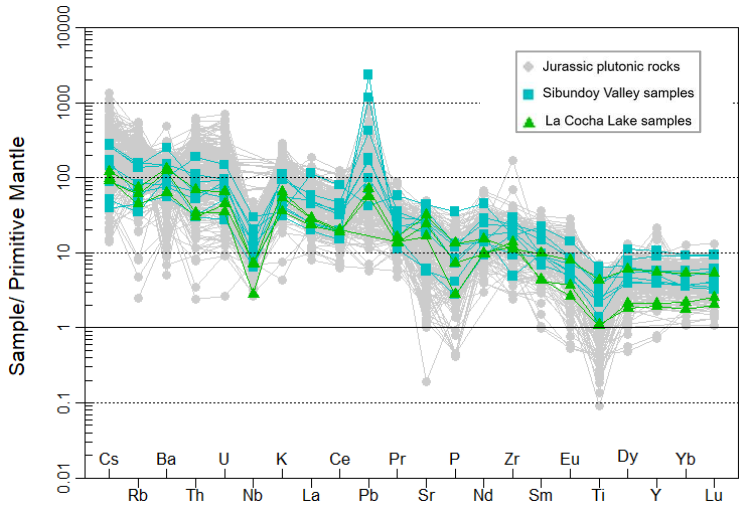

Figure 11. Multi-element plot normalized to primitive mantle according to Sun and McDonough (1989).

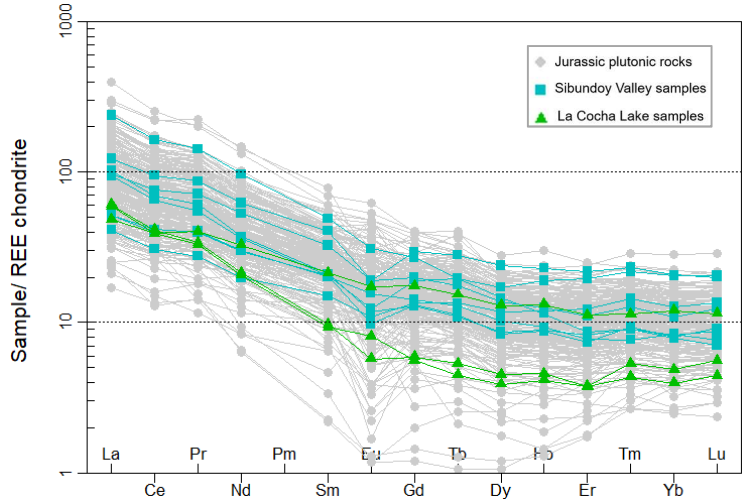

Figure 12. Chondrite normalized REE patterns, according to Nakamura (1974).

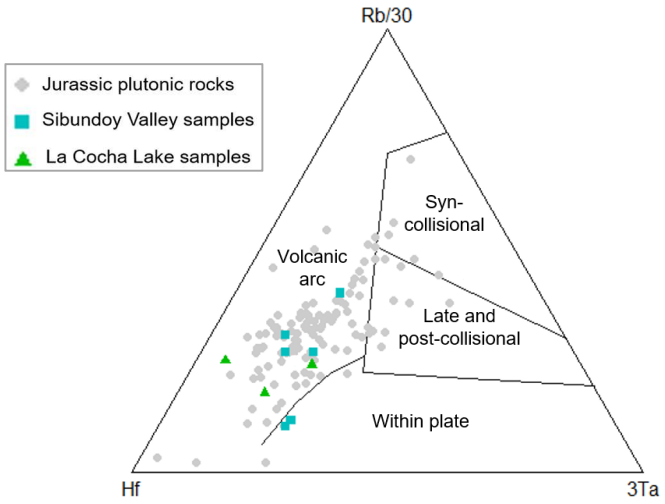

Figure 13. Discrimination diagram of granites (Hf-Rb/30-Ta*30), according to Harris et al. (1986).

4.2.2. Metamorphic rocks

SiO_2 values of samples JC003B and JC007 lay between 46.1 wt % and 63.8 wt %, Al_2O_3 ranges from 15.1 wt % to 17.5 wt %, Na_2O varies from 1 wt% to 3.3 wt%, CaO contents are high (0.5-6.4 wt %), MgO shows variable values (1.7-5.2 wt %), and K_2O values are intermediate (1.7-4.6 wt %).

The diagram classification of volcanic rocks of Winchester and Floyd (1977) (Fig.14) was used to constrain the protolith of these samples, which plot in the Andesite/Basalt (JC007) and subalkaline basalts (JC003B).

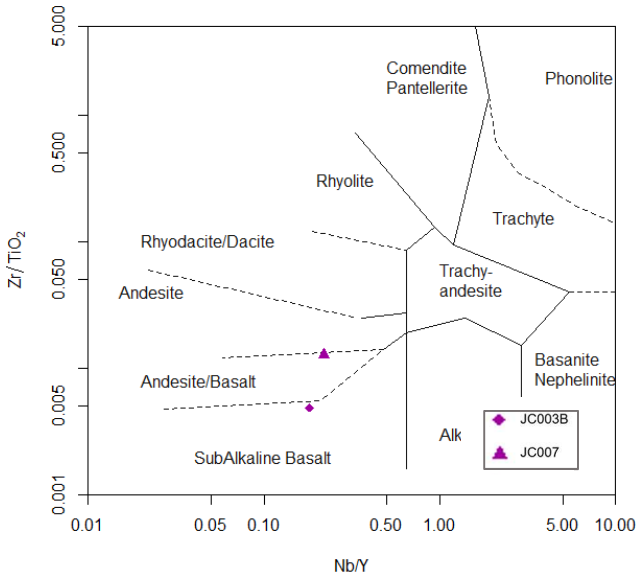

Figure 14. Diagram classification of volcanic rocks based on immobile elements rations of Nb/Y vs. Zr/Ti (Winchester and Floyd, 1977)

Multi-element diagram normalized to the primitive mantle (Sun & McDonough, 1989; Fig. 15) shows negative anomalies of Nb, and positive anomalies of Pb, and K.

As shown in the REE diagram normalized to chondrite according to Nakamura (1974) (Fig. 16) the rocks have a slightly steep REE pattern ((La/Yb)N= 3.4-3.8), show an enrichment in LREE compared with HREE ((La/Sm)N= 1.4-2.3, (Tb/Yb)N= 1.1-1.9), the LREE-MREE slope is negative ((La/Dy)N= 2.6-3.3), and the MREE-HREE slope is flat-shaped ((Dy/Yb)N= 1.1-1.5). Eu anomaly is absent (Eu/Eu*= 1.0).

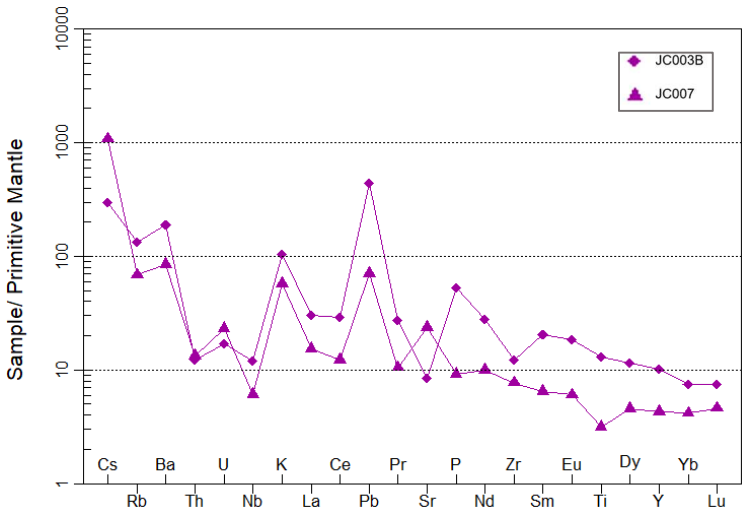

Figure 15. Multi-element plot normalized to primitive mantle, according to Sun and McDonough (1989).

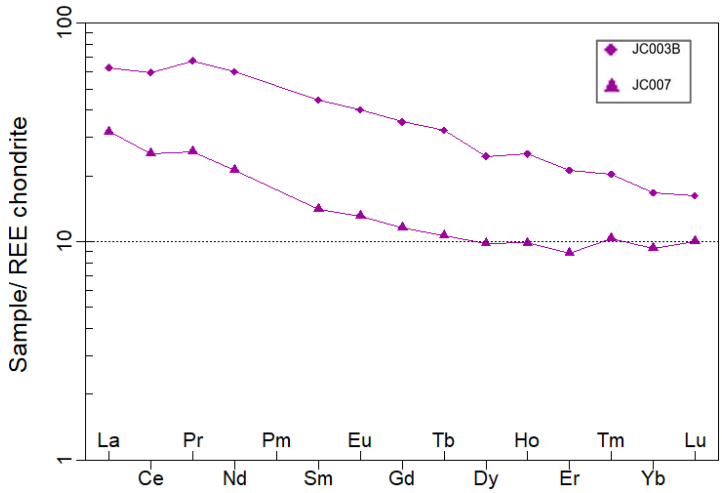

Figure 16. Chondrite normalized REE patterns, according to Nakamura (1974).

4.3. Geochronology

U-Pb zircon analyses were realized for four samples from the northeast of the Sibundoy Valley and the west of La Cocha Lake. Three samples are igneous rocks (samples JC001, JC014A, JC016), which varies from diorite to granite, and one sample (JC003B) is hornblende-biotite schist. Analytical results are presented in Table 2 (see appendix).

4.3.1. Plutonic rocks

Zircons of sample JC001 (granite) range from 50 to 150 µm in length. They are mainly stubby and subhedral crystals. Cathodoluminescence (CL) images (Fig. 17) shows that some crystals at the rim zones display faint oscillatory zonation, and present U-rich metamict cores. Th/U ratios of the crystals vary from 0.1 to 3.8, suggesting that they are magmatic zircons (Rubatto, 2002). U-Pb analyses were performed on twenty-four zircon grains (thirty-six spots done in both cores and rims). After removing from the calculation zircons with >10% discordance, the analysis provided a Tuff Zircon age of 174.50 +2.70 -2.20 Ma (Fig. 18).

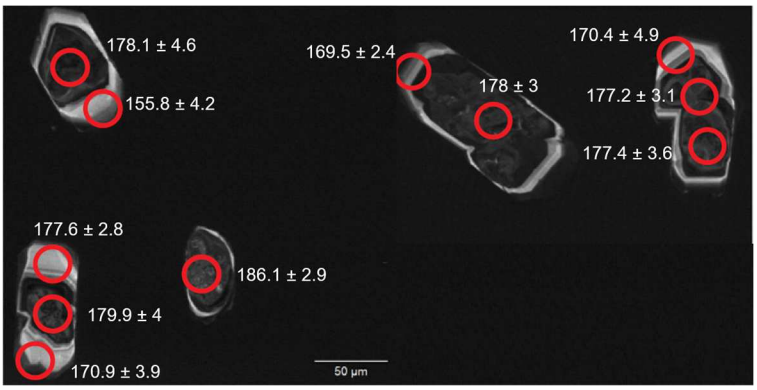

Figure 17. Cathodoluminescence (CL) images from selected zircons of the sample JC001 showing the analyzed spots and U-Pb ages obtained.

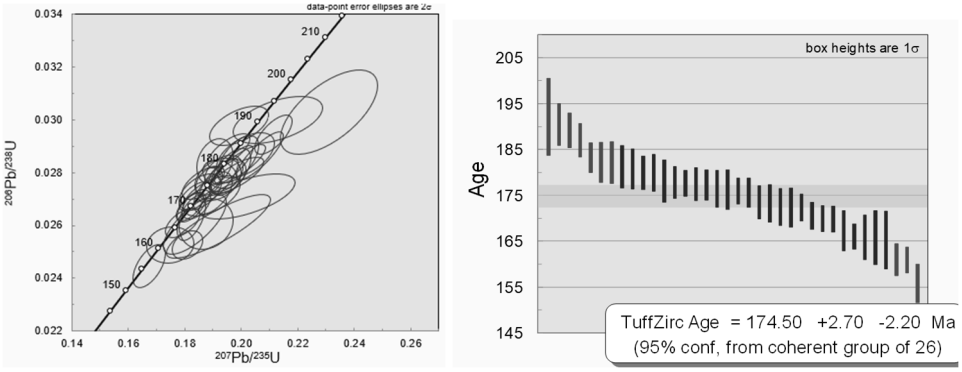

Figure 18. Concordia with 2σ box heights and Tuff Zircon age of sample JC001

Zircons grains of sample JC014A (diorite) range from 35 to 110 µm in length. They are stubby anhedral crystals with subrounded and rounded terminations. Cathodoluminescence images shows that are zoned zircons (Fig. 19). Th/U ratios of the crystals vary from 0.2 to 1.0; this suggests that they are magmatic zircons (Rubatto, 2002). U-Pb analyses were performed on eighteen grains (twenty-seven spots done in both cores and rims). After removing from the calculation zircons with >10% discordance, the analysis provided a Tuff Zircon age of 153.45 +1.45 -2.05 Ma (Fig. 20).

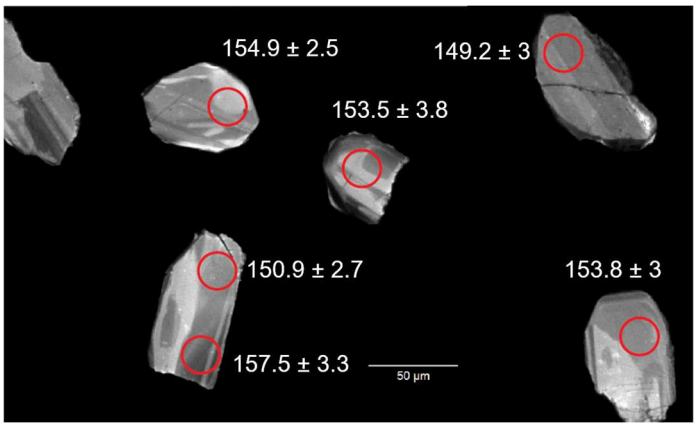

Figure 19. Cathodoluminescence (CL) images from selected zircons of the sample JC014A showing the analyzed spots and U-Pb ages obtained.

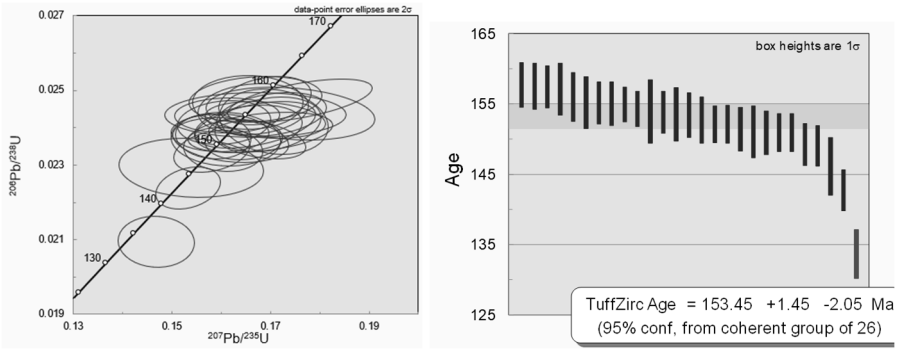

Figure 20. Concordia with 2σ box heights and Tuff Zircon age of sample JC014A.

Sample JC016 (granite) present Th/U ratios that vary from 1.1 to 2.0; this suggests that they are magmatic zircons (Rubatto, 2002). U-Pb analyses were performed on (thirty-seven spots done in both cores and rims). After removing from the calculation zircons with >10% discordance, the analysis provided a Tuff Zircon age of 152.05 + 1.56 – 0.87 Ma (Fig. 21).

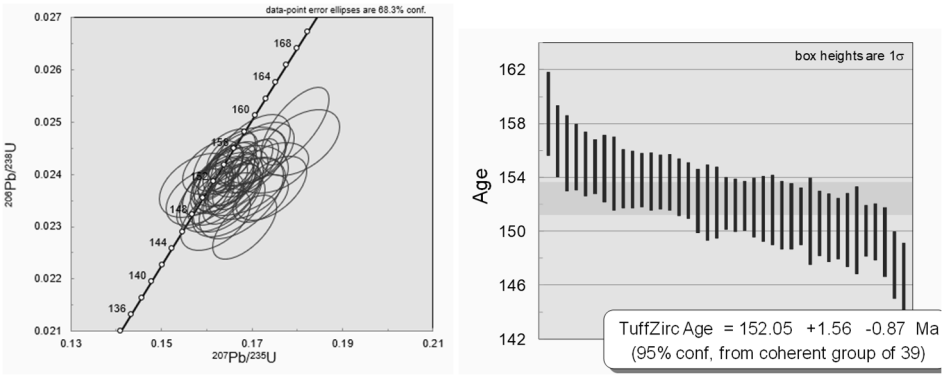

Figure 21. Concordia with 1σ box height with 68.3% confidence error ellipses and Tuff Zircon age of sample JC016.

4.3.2. Metamorphic rocks

The analyzed zircon grains of the hornblende-biotite schist (sample JC003B) range from 50 to 100 μm in length and are stubby and subhedral crystals. CL images show absence or thin metamorphic overgrowths, and some crystals present xenocrystic cores (Fig. 22). Th/U ratios of the crystals vary from 0.2 to 0.6, suggesting that they are magmatic zircons (Rubatto, 2002). U-Pb analyses were performed on six zircon grains (twelve spots done in both cores and rims). After removing from the calculation zircons with >10% discordance, the analysis provided a Tuff Zircon age of 167.7 +10.1 -2.7 Ma. These results indicate that the zircons record the age of the igneous crystallization of the protolith (Fig. 23).

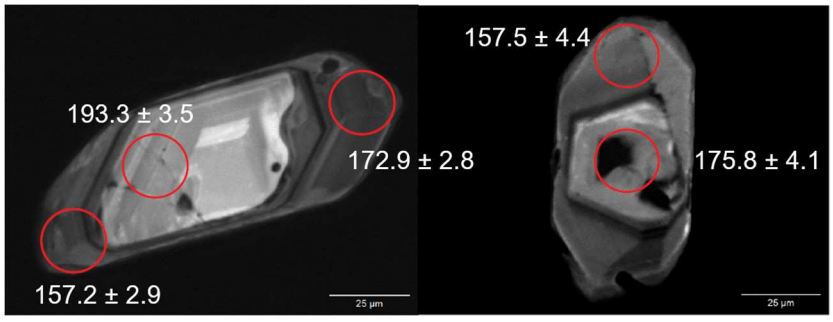

Figure 22. Cathodoluminescence (CL) images from selected zircons of the sample JC003B showing the analyzed spots and U-Pb ages obtained.

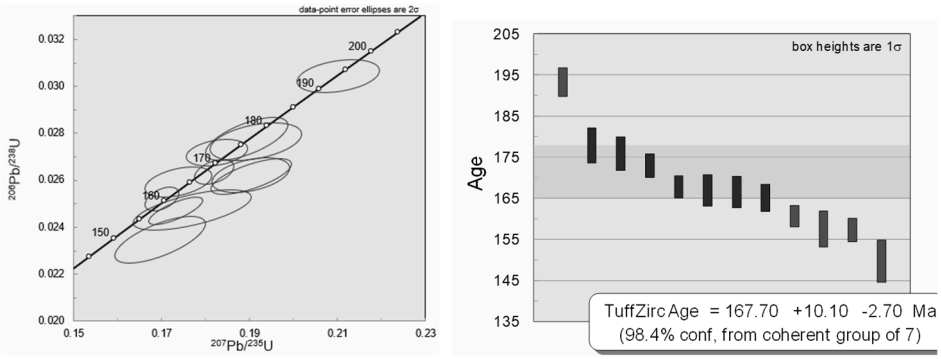

Figure 23. Concordia with 2σ box heights and Tuff Zircon age of sample JC003B.

5. Discussion

5.1. Timing and origin of the magmatism

U-Pb zircon ages of the magmatic rocks indicate that they crystallized during two different time intervals. Samples analyzed from the Sibundoy Valley yielded a crystallization age of ca.174 Ma that corresponds to the Middle Jurassic, similar crystallization ages have been obtained at the southern part of the Central Cordillera, the San Lucas Massif (Leal-Mejía, 2019), the Garzón Massif (García, 2018), and in the Upper Magdalena Valley (Bustamante et al., 2010). Samples from La Cocha Lake yielded ages of ca. 152 Ma that correspond to the Late Jurassic, these results are comparable with ages reported by Bustamante et al., (2016) in the north of Ibagué (Central Cordillera; Fig. 24, 25).

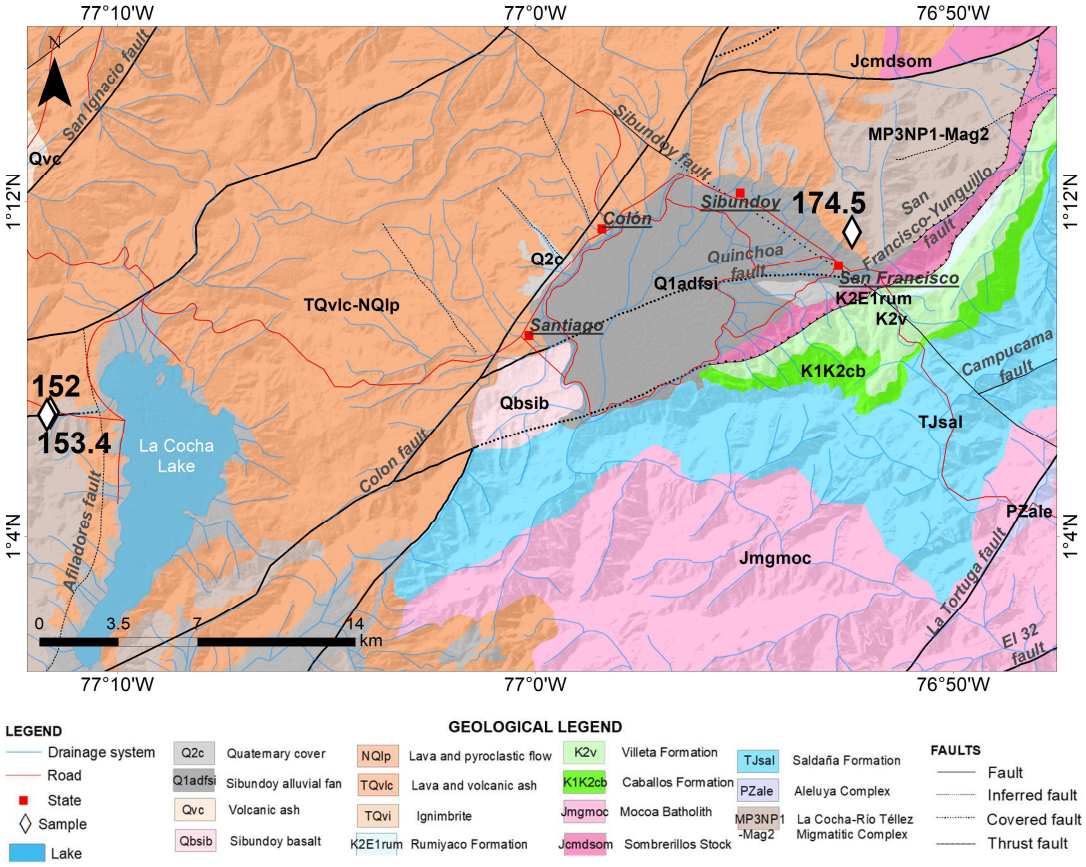

LEGEND

- Drainage system
- Road
- State
- Sample
- Lake

GEOLOGICAL LEGEND

Q2c	Quaternary cover	NQlp	Lava and pyroclastic flow	K2v	Villeta Formation	TJsal	Saldaña Formation
Q1adfsi	Sibundoy alluvial fan	TQvlc	Lava and volcanic ash	K1K2cb	Caballos Formation	PZale	Aleluya Complex
Qvc	Volcanic ash	TQvi	Ignimbrite	Jmgmoc	Mocoa Batholith	MP3NP1-Mag2	La Cocha-Río Téllez Migmatitic Complex
Qbsib	Sibundoy basalt	K2E1rum	Rumiyaco Formation	Jcmdsom	Sombrerillos Stock		

FAULTS

- Fault
- Inferred fault
- Covered fault
- Thrust fault

Figure 24. Geological map of the study area with samples JC001, JC014A, and JC016 location, and their U-Pb age.

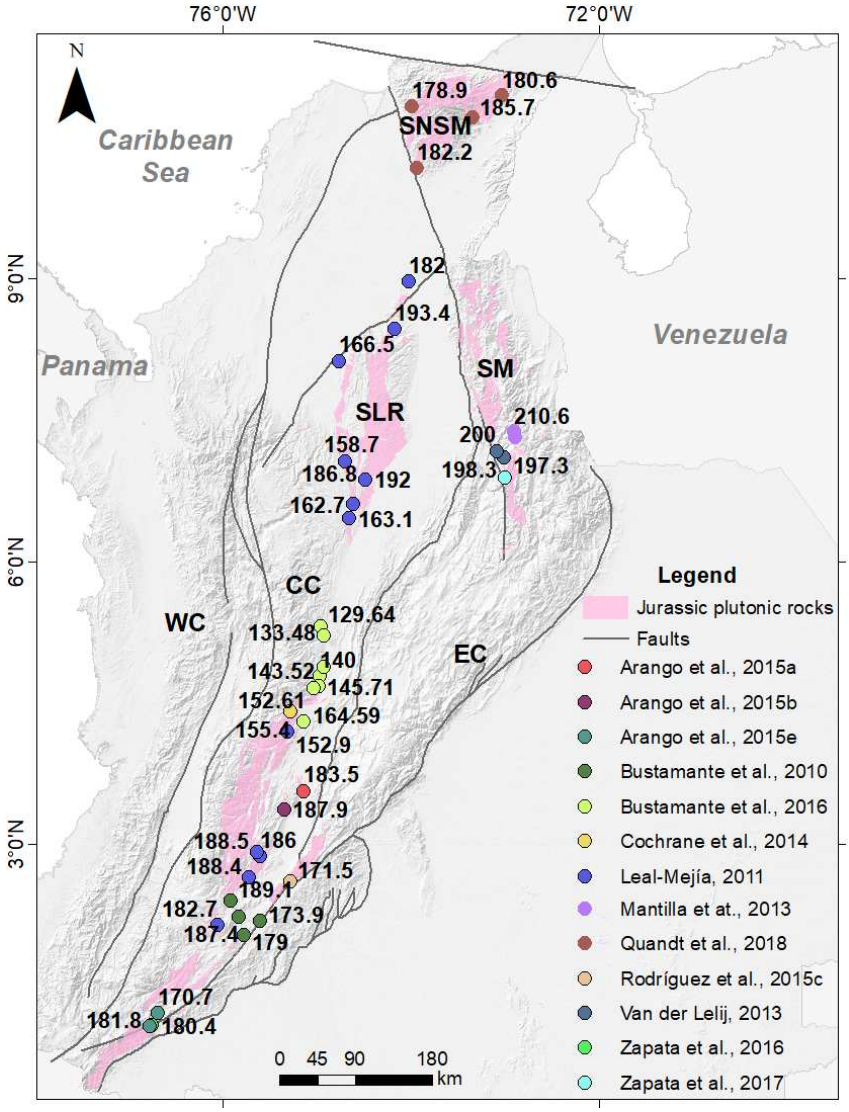

Figure 25. Distribution of Jurassic magmatism in Colombia. **SNSM**: Sierra Nevada de Santa Marta; **SLR**: San Lucas Range; **SM**: Santander Massif; **WC**: Western Cordillera; **CC**: Central Cordillera**; EC:** Eastern Cordillera.

These U-Pb crystallization ages are within the time interval reported for the duration of the Jurassic magmatic belt of the Central Cordillera, whose earliest ages are of ca. 189 Ma (Bustamante et al., 2010) whereas the youngest is of ca. 129 Ma (early Cretaceous; Bustamante et al., 2016). Although there is an apparent westward migration of the magmatism (Figure 1C), as has been proposed in recent works (i.e. Cochrane et al., 2014; Spikings et al., 2015; 2019), this pattern is precluded when the crystallization ages are compared with the whole magmatic record of the Central Cordillera (Cadavid and Madrid, 2019), rendering difficult to explain

why the migration pattern is not repeated in other segments of the Jurassic magmatic belt. Even an eastward migration based on the distribution of U-Pb ages has been proposed (Rodríguez et al., 2018), although this model has been challenged by Bustamante et al. (2019) because the isotopic constraints have not been considered. The timing of the magmatism that is being recorded here also coincides with the period of decreasing magma volumes proposed by Bustamante et al. (2016) and that is also seen in the data reported by Leal-Mejía et al. (2019). However, the absence of adequate geological mapping of the La Cocha area makes it difficult to evaluate if the youngest pulse of magma recorded is less voluminous than the older.

The tectonic setting of this magmatism can be constrained based on the whole rock geochemistry. Trace element concentrations show relative enrichment of LILE and LREE compared with HFSE and HREE respectively, negative anomalies of Nb and Ti, and positive anomalies of K, Ba, and Pb; these patterns indicate that continental crust was involved during the magma genesis, which demonstrates that these rocks were formed in a volcanic-arc setting, this is also confirmed by tectonic discrimination diagrams (Harris et al., 1986). These patterns are observed for other Jurassic magmatic rocks in Colombia; thus, it can be assumed that the samples found in southern Colombia and rocks of the Jurassic magmatic arc share similar assimilation process and were formed in the same tectonic setting.

Petrographic analyses allow us to recognize mineralogical, compositional and microstructural variations; the eastern part of the studied zone (Sibundoy Valley) is composed of intermediate, medium grain size rocks constituted by quartz, plagioclase, microcline, biotite, and hornblende, and microstructures like microcline twinning, bent plagioclase (deformed twins), myrmekite, undulatory extinction and chess-board pattern in quartz, while

the western part (La Cocha Lake) is composed of felsic, medium grain size and highly deformed rocks constituted mostly of quartz, plagioclase, and potassium feldspar with minor contents of biotite and hornblende, and presents microstructures like chess-board pattern in quartz and quartz recrystallization. These microstructures are evidence of solid-state deformation, which indicate that the rocks underwent deformation at high-temperature at 700-800 °C (Vernon, 2004; Nédélec & Bouchez, 2015). Similar deformational patterns have been recognized in the northernmost segment of the Ibagué batholith, in samples located at its western margin and with similar reported crystallization ages (ca. 152 Ma) Bustamante et al. (2016). In that sense, it is possible to speculate that the causes of such deformational patterns are more regional, possibly related to the metamorphic jurassic rocks located to the west (Blanco-Quintero et a., 2014; Bustamante et al., 2017). However, a more detailed microstructural work is needed, in order to make more precise interpretations.

5.2. Metamorphic conditions and possible correlations

The hornblende-biotite schists found in the study area, allow us to define that they were metamorphosed under amphibolite facies conditions. Despite the fact that for this study were not calculated P-T projections, it can thus be suggested that these rocks were approximately formed at temperatures between 550 to 700 °C, pressures that vary from 0.2 to 1 GPa, and depths between 10 and 35 Km; these conditions are typical of intermediate P/T metamorphic rocks, which underwent regional metamorphism (Bucher & Grapes, 2011). Similar P-T conditions were reported by Blanco-Quintero et al., (2014) in metapelites and amphibolites from the Central Cordillera (i.e. Cajamarca Complex).

Blanco-Quintero et al. (2014) obtained precise P-T-t paths that were interpreted as the collision of the Permo-Triassic basement of the Central

Cordillera (Tahami terrane) with the northwestern margin of South America, west to the Jurassic batholiths. According to these authors, peak metamorphic conditions reached 550 to 580 °C and 0.8 GPa during Late Jurassic (146 to 158 Ma). Bustamante et al. (2017) obtained inherited detrital zircon ages in metapelites from the same metamorphic complex with a peak age of ca. 162 Ma, and Zapata-García et al. (2017) reported metamorphic ages from La Cocha-Río Tellez Migmatitic Complex of ca. 163 Ma. This may suggest a possible Jurassic metamorphic complex along the Central Cordillera and even extending into the Cordillera Real in Ecuador (Bustamante et al., 2017; Blanco-Quintero et al., 2014).

The hornblende-biotite schists yielded a U-Pb in zircon age of ca. 167 Ma; although this age is considered the crystallization age of the protolith, it is similar to the ages reported in Bustamante et al. (2017) for a metapelite of the Cajamarca Complex (Fig. 26, 27). Comparing the preliminary metamorphic conditions described in this study with those reported north by Blanco-Quintero et al. (2014), the schists from Sibundoy Valley were formed by the same metamorphic event after the Middle Jurassic, that has been previously reported in other localities along the Central Cordillera (Blanco-Quintero et al., 2014; Bustamante et al., 2017; Zapata-García et al., 2017). However, more geochronology, as well as metamorphic information, is needed to constrain and define the limits of this possible Jurassic metamorphic belt.

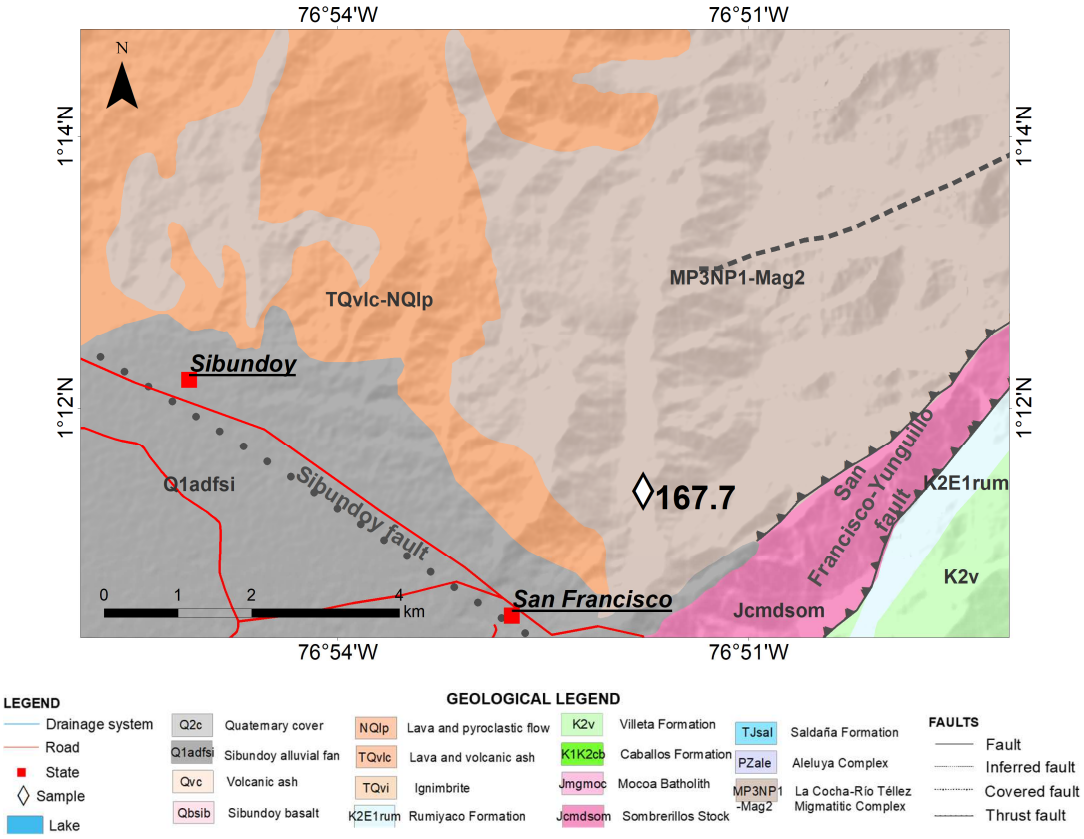

Figure 26. Geological map of the study area in the Sibundoy Valley with sample JC003B location and its U-Pb age.

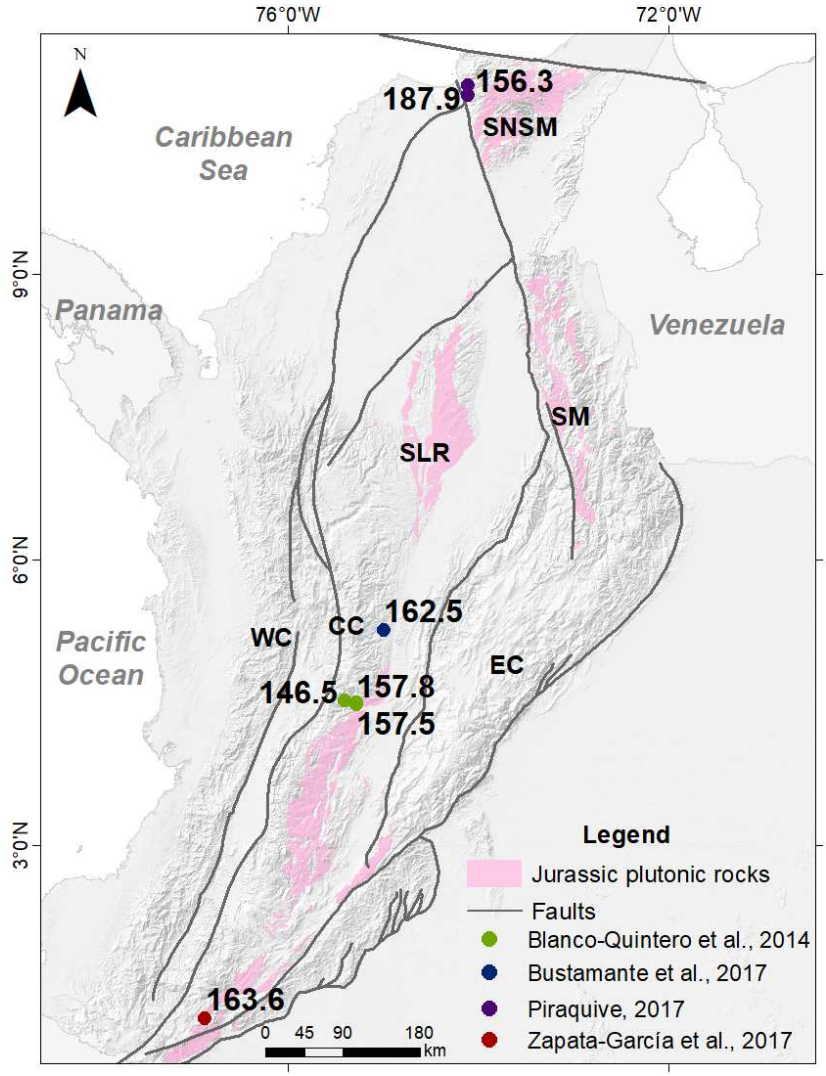

Figure 27. Distribution of Jurassic metamorphism in Colombia. **SNSM**: Sierra Nevada de Santa Marta; **SLR**: San Lucas Range; **SM**: Santander Massif; **WC**: Western Cordillera; **CC**: Central Cordillera**; EC:** Eastern Cordillera.

5.3. Tectonic implications

The slab roll-back model proposed by Cochrane et al. (2014) and Spikings et al. (2015) indicates that the Jurassic magmatic arc of the Northern Andes underwent westward migration since 190 Ma until 105 Ma. However, this model does not consider evidence like the decreasing magmatic activity after 165 Ma and the lack of a clear age migration between 190 Ma and

129 Ma along the Central Cordillera (Bustamante et al., 2016; Cadavid and Madrid, 2019).

Additionally, slab roll-back has been considered a process that allows the exhumation of HP/UHP metamorphic rocks (Brun and Faccenna, 2008), but it does not explain the formation of an intermediate P/T metamorphic belt as the reported for the Northern Andes (Blanco-Quintero et al., 2014; Zapata-García et al., 2017), neither its fault contact with Jurassic igneous rocks (Blanco-Quintero et al., 2014, this work).

Previous research has established that the decrease in the magmatic production, the lack of arc migration, and the formation of a medium P/T metamorphic belt in the Northern Andes could be explained by translation of terranes in an oblique convergence along the northwestern margin of South America (Bayona et al., 2016; 2010; Bustamante et al., 2016; Blanco-Quintero et al., 2014; Bustamante et al., 2017), where the oblique converge produced a magmatic stationary arc causing a long-term evolution of the magma sources (Bustamante et al., 2016), and allow the translation of para-autochthonous terranes that triggered regional metamorphism, which form the rocks found in the Central Cordillera and in southern Colombia (Blanco-Quintero et al., 2014; Zapata-García et al., 2017, this work). This scenario would be more accurate and allow us to integrate both magmatic and metamorphic rocks in the same tectonic model.

6. Conclusions

Regional correlations allow us to identify that the rocks found in southern Colombia are part of the Jurassic magmatic arc, and they are part of a collisional event occurred in the Late Jurassic; likewise, it could be said that the Jurassic metamorphic belt extends to the south of Colombia and is

tectonically related with the Jurassic magmatic arc. Additionally, this enables us to suggest that these tectono-magmatic and metamorphic events are related to the translation of terranes in an oblique convergence along the northwestern margin of South America.

Although the interpretations may be somewhat limited by number of samples, the lack of a systematic sampling method that let us recognize detailed compositional and age variations, and the limited methods used for petrological metamorphic analysis, this work contribute to the development of knowledge about the Jurassic in the southern Colombia, which is a poorly studied region, and is an approximation to understand the relation between the Jurassic magmatic arc and the metamorphic belt of the Northern Andes.

References

Arango, M.I., Rodríguez, G., Zapata, G., Bermúdez, J.G., 2015. Catálogo de unidades litoestratigráficas de Colombia: Monzogranito de Mocoa, Cordillera Oriental, Departamentos Putumayo, Huila, Cauca y Nariño. Servicio Geológico Colombiano.

Aspden, J.A., McCourt, M.J., Brook, M., 1987. Geometrical control of subduction-related magmatism: the Mesozoic and Cenozoic plutonic history of Western Colombia. Journal of the Geological Society 144, 893-905.

Bayona, G.A., Bustamante, C., Nova, G. and Salazar-Franco, A.M. (2019). Jurassic evolution of the northwestern corner of Gondwana: Present knowledge and future challenges in studying Colombian Jurassic rocks. The geology of Colombia book. Volume 2. Chapter 5. 101–132.

Black, L. P., Kamo, S. L., Allen, C. M., Aleinikoff, J. N., Davis, D. W., Korsch, R. J., & Foudoulis, C. 2003. TEMORA 1: a new zircon standard for Phanerozoic U–Pb geochronology. Chemical Geology, 200 (1): 155-170.

Blanco–Quintero, I.F., García–Casco, A., Toro, L.M., Moreno, M., Ruiz, E.C., Vinasco, C.J., Cardona, A., Lázaro, C. & Morata, D. 2014. Late Jurassic terrane collision in the northwestern margin of Gondwana (Cajamarca Complex, eastern flank of the Central Cordillera, Colombia). International Geology Review 56(15): 1852–1872. Doi: 10.1080/00206814.2014.963710

Bustamante, C., Cardona, A., Bayona, G., Mora, A., Valencia, V., Gehrels, G., Vervoort, J., 2010. U-Pb LA-ICP-MS geochronology and regional correlation of Middle Jurassic intrusive rocks from the garzon massif, Upper Magdalena Valley and Central Cordillera, Southern Colombia. Boletín de Geología 32, 93-109.

Bustamante, C., Archanjo, C.J., Cardona, A., Vervoort, J.D., 2016. Late Jurassic to Early Cretaceous plutonism in the Colombian Andes: a record of long-term arc maturity. Geological Society of America Bulletin 128, 1762–1779.

Bustamante, C., Archanjo, C.J., Cardona, A., Bustamante, A. & Valencia, V., 2017. U–Pb ages and Hf isotopes in zircons from parautochthonous Mesozoic terranes in the western margin of Pangea: Implications for the terrane configurations in the Northern Andes. The Journal of Geology 125(5): 487–500. doi: 10.1086/693014

Bustamante, C., Cardona, A., Bustamante, A., Vanegas, J., 2019. Comment on 'Petrotectonic characteristics, geochemistry, and U-Pb geochronology of Jurassic plutons in the Upper Magdalena Valley-Colombia: Implications on the evolution of magmatic arcs in the NW Andes' by Rodríguez et al. (2018).

Cadavid, C., and Madrid, L., 2019. Análisis de las variaciones en la distribución, profundidad y fuente de las rocas plutónicas Jurásicas de la Cordillera Central de Colombia y sus implicaciones en la evolución del Norte de los Andes (Tesis de pregrado). Universidad EAFIT, Medellín, Antioquia.

Cediel, F., R. P. Shaw, and C. Cáceres, 2003, Tectonic assembly of the Northern Andean Block, in C. Bartolini, R. T. Buffler, and J. Blickwede, eds., The Circum-Gulf of Mexico and the Caribbean: Hydrocarbon habitats, basin formation, and plate tectonics: AAPG Memoir 79, p. 815– 848.

Cochrane, R., Spikings, R., Gerdes, A., Winkler, W., Ulianov, A., Mora, A., Chiaradia, M., 2014. Distinguishing between in-situ and accretionary growth of continents along active margins. Lithos 202-203, 382-394.

Cortés, M., Colletta, B., Angelier, J., 2006. Structure and tectonics of the central segment of the Eastern Cordillera of Colombia. Journal of South American Earth Sciences 21, 437–465.

Harris, N.W., Pearce, J.A., and Tindle, A.G. 1986. Geochemical characteristics of collision-zone magmatism. Geological Society of London, Special Publication., 19: 67-81.

Jiménez-Mejía, D.M., 2003. Metamorphic and geochronological characterization of the proterozoic rocks of the Garzón massif - southeast of the Colombian Andes. Universidade de São Paulo, Instituto de geociências. São Paulo.

Ducea, M.N., Saleeby, J.B., Bergantz., G., 2015. The Architecture, Chemistry, and Evolution of Continental Magmatic Arcs. Annual Review of Earth and Planetary Sciences 2015 43:1, 299-331. Doi: 10.1146/annurev-earth-060614-105049

Fennstra, A., Franz, G., 2015. Regional Metamorphism. Reference Module in Earth Systems and Environmental Sciences. Doi:10.1016/b978-0-12-409548-9.09547-6

García, D.A., 2018. Petrogénesis y evolución tectónica de rocas graníticas de la región de Garzón, Cordillera Oriental de Colombia. (Tesis Doctorado). Universidade de São Paulo, Instituto de geociências. São Paulo.

Guillong, M., von Quadt, A., Sakata, S., Peytcheva, I. &Bachmann, O. 2014. LA-ICP-MS Pb-U dating of young zircons from the Kos-Nisyros volcanic cente, SE Aegean arc. J. Anal. At. Spectrom., 29, 963, DOI: 10.1039/c4ja00009a.

Jackson, S. E., Pearson, N. J., Griffin, W. L., & Belousova, E. A. 2004. The application of laser ablation-inductively coupled plasma-mass spectrometry to in situ U–Pb zircon geochronology. Chemical Geology, 211(1), 47-69

Janoušek, V., Farrow, C.M., Erban, V., 2006. Interpretation of whole-rock geochemical data in igneous geochemistry: introducing Geochemical Data Toolkit (GCDkit). J. Petrol. 47 (6), 1255–1259.

Hinton, R. W. 1999. NIST SRM 610, 611 and SRM 612, 613 Multi-Element Glasses: Constraints from Element Abundance Ratios Measured by Microprobe Techniques. Geostandards Newsletter, 23 (2): 197-207

Leal-Mejía, H., Shaw, R.P. and Melgarejo, J.C., 2019. Spatial-Temporal Migration of Granitoid Magmatism and the Phanerozoic Tectono-Magmatic Evolution of the Colombian Andes. Geology and Tectonics of Northwestern South America. Part IV. Chapter 5. 253- 254.

Ludwig, K., 2012, User's Manual for Isoplot 3.75 A Geochronological Toolkit for Microsoft Excel, Berkeley, CA, Berkeley Geochronological Center Special Publication No. 5.

Middlemost, E. 1994. Naming materials in magma/igneous rock system. Earth Sci Rev 37:215–224

Mora, A., Gaona, T., Kley, J., Montoya, D., Parra, M., Quiroz, L., Reyes, G., and Strecker, M. 2009. The Role of inherited extensional fault segmentation and linkage in contractional orogenesis: a reconstruction of Lower Cretaceous inverted rift basins in the Eastern Cordillera of Colombia. Basin Research 21, 111-137.

Nakamura, N., 1974. Determination of REE, Ba, Fe, Mg, Na and K in carbonaceous and ordinary chondrites. Geochimica et Cosmochimica Acta, 38: 757-775.

Nédélec, A., Bouchez, J.-L., 2015. Granites: Petrology, Structure, Geological Setting and Metallogeny. Oxford University Press, p. 335.

Núñez, A., 2003. Reconocimiento geológico regional de las planchas 411 La Cruz, 412 San Juan de Villalobos, 430 Mocoa, 431 Piamonte, 448 Monopamba, 449 Orito y 465 Churuyaco Departamentos de Caquetá, Cauca, Huila, Nariño y Putumayo Escala 1:100.000 Memoria Explicativa. INGEOMINAS. 92-98.

Paterson, S.R., Vernon, R.H., Tobisch, O.T., 1989. A review of criteria for the identification of magmatic and tectonic foliations in granitoids. Journal of Structural Geology. 11, 349-364.

Paton, C., Hellstrom, J., Paul, B., Woodhead, J., Hergt, J. 2011. Iolite: Freeware for the visualisation and processing of mass spectrometric data. J. Anal. At. Spectrom., 26: 2508, DOI: 10.1039/c1ja10172b.

Peccerillo A., Taylor, T.S., 1976. Geochemistry of Eocene calc-alkaline volcanic rocks from Kastamonu area, Northern Turkey. Contributions to Mineralogy and Petrology, 58, 63-81.

Petrus, J.A. and Kamber, B.S. 2012. VizualAge: A Novel Approach to Laser Ablation ICP-MS U-Pb Geochronology Data Reduction. Geostandards and Geoanalytical Research, 36: 247-270

Piraquive, A. 2016. Marco estructural deformaciones y exhumación de los Esquistos de Santa Marta: La acreción e historia de deformación de un terreno Caribeño al norte de la Sierra Nevada de Santa Marta. Doctorade thesis, Université Grenoble Alpes & Universidad Nacional de Colombia, 394 p. Bogotá.

Quandt, D., Trumbull, R., Altenberger, U., Cardona, A., Romer, R., Bayona, G., Ducea, M., Valencia, V., Vásquez, M., Cortes, E., Guzman, G., 2018. The geochemistry and geochronology of Early Jurassic igneous rocks from the Sierra Nevada de Santa Marta, NW Colombia, and tectono -magmatic implications. Journal of South American Earth Sciences 86, 216-230.

Rodríguez, G., Arango, M., Zapata, G., Bermúdez, J., 2016. Catálogo de unidades litoestratigráficas de Colombia: Formación Saldaña, Cordillera Central y Oriental, Tolima, Huila, Cauca y Putumayo. Servicio geológico colombiano.

Rodríguez, G., Arango, M.I., Zapata, G., Bermúdez, J.G., 2018. Petrotectonic characteristics, geochemistry, and U-Pb geochronology of Jurassic plutons in the Upper Magdalena Valley-Colombia: Implications on the evolution of magmatic arcs in the NW Andes. Journal of South American Earth Sciences 81, 10-30.

Rubatto, D. 2002. Zircon trace element geochemistry: partitioning with garnet and the link between U-Pb ages and metamorphism. Chem. Geol. 184:123–138.

Shand, S. J., 1943. Eruptive Rocks. Their Genesis, Composition, Classification, and Their Relation to Ore-Deposits with a Chapter on Meteorite. New York: John Wiley & Sons.

Sláma, J., Košler, J., Condon, D. J., Crowley, J. L., Gerdes, A., Hanchar, J. M., Horstwood, M. S. A., Morris, G. A., Nasdala, L., Norberg, N., Schaltegger, U., Schoene, B., Tubrett., M. N., Whitehouse, M. J. 2008. Plešovice zircon—a new natural reference material for U–Pb and Hf isotopic microanalysis. Chemical Geology, 249 (1), 1-35.

Spikings, R., Cochrane, R., Villagomez, D., van der Lelij, R., Vallejo, C., Winkler, W., Beate, B., 2015. The geological history of northwestern South America: from Pangaea to the early collision of the Caribbean large igneous province (290–75 Ma). Gondwana Research 27, 95–139.

Spikings, R., Cochrane, R., Vallejo, C., Villagómez, D., Van der Lelij, R., Paul, A., Winkler, W., 2019. Latest Triassic to Early Cretaceous tectonics of the Northern Andes: Geochronology, geochemistry, isotopic tracing, and thermochronology. Andean Tectonic. Chapter 7. 173-208.

Sun, S.S., McDonough, W.F., 1989. Chemical and isotopic systematics of oceanic basalts: implications for mantle composition and processes. En Sanders, A.D., Norry, M.J. (Eds.). Magmatism in oceanic basins. Geological Society of London, Special Publication, 42, 313 – 345.

Vásquez, M., Altenberger, U., Romer, R.L., Sudo, M., Moreno-Murillo, J.M., 2010. Magmatic evolution of the Andean Eastern Cordillera of Colombia during the Cretaceous: Influence of previous tectonic processes. Journal of South American Earth Sciences. 2, 171-186. Doi: 10.1016/j.jsames.2009.02.003

Vernon, R.H., 2004. A Practical Guide to Rock Microstructure. Cambridge University Press, Cambridge.

Villagómez, D., Spikings, R., Magna, T., Kammer, A., Winkler, W., Beltrán, A., 2011. Geochronology, geochemistry and tectonic evolution of Western and Central Cordilleras of Colombia. Lithos 125, 875–896.

Vinasco, C., Cordani, U., González, H., Weber, M., Peláez, C., 2006. Geochronological, isotopic, and geochemical data from Permo-Triassic granitic gneisses and granitoids of the Colombian Central Andes. Journal of South American Earth Sciences 21, 355-371.

Von Quadt, A., Wotzlaw, J.-F., Buret, Y., Large, S.J.E., Peytcheva, I., Trinquir, A. 2016. High-precision zircon U/Pb geochronology by ID-TIMS using new 1013 ohme resistors. J. Anal. At. Spectrom., 31, 658, DOI: 10.1039/c5ja00457h.

Wiedenbeck, M., Alle, P., Corfu, F., Griffin, W. L., Meier, M., Oberli, F., von Quadt, A., Roddick, J. C., Spiegel, W. 1995. 3 natural zircon standards for U-Th-Pb, Lu-Hf, trace-element and REE analyses. Geostandards Newsletter 19: 1–23

Winchester, J.A., Floyd, P.A., 1977. Geochemical discrimination of different magma series and their differentiation products using immobile elements. Chemical Geology 20, 325–343

Winter, J.D., 2014. Principles of Igneous and Metamorphic Petrology. 2nd Edition. Pearson.

Zapata., S., Cardona, A., Jaramillo, C., Valencia, V., and Vervoort, J. 2016. U-Pb LA-ICP-MS geochronology and geochemistry of Jurassic volcanic and plutonic rocks from the Putumayo region (southern Colombia): tectonic setting and regional correlations. Boletín de Geología 38, 21-38.

Zapata, S., Cardona, A., Jaramillo, J.S., Patiño, A., Valencia, V., León, S., Mejía, D., Pardo-Trujillo, A., Castañeda, J.P., 2019. Cretaceous extensional and compressional tectonics in the Northwestern Andes, prior to the collision with the Caribbean oceanic plateau. Gondwana Research 66, 207-226.

Zapata-García, G., Rodríguez, G., Arango, M.I., 2017. Petrografía, geoquímica y geocronología de rocas metamórficas aflorantes en San Francisco Putumayo y la vía Palermo-San Luis asociadas a los complejos La Cocha – Río Téllez y Aleluya Boletín de Ciencias de la Tierra 41, 47-64.

Zheng, Yong-Fei., Chen, Yi-Xiang., 2016. Continental versus oceanic subduction zones. National Science Review. 3. 495-519. Doi: 10.1093/nsr/nww049.

Zuluaga, C.A., Amaya, S., Urueña, C. & Bernet, M., 2017. Migmatization and low–pressure overprinting metamorphism as record of two pre–Cretaceous tectonic episodes in the Santander Massif of the Andean basement in northern Colombia (NW South America). Lithos, 274–275: 123–146. Doi: 10.1016/j.lithos.2016.12.036

Appendix

Table 1.Whole-rock analyses of samples from the Sibundoy Valley and La Cocha Lake.

	Sibundoy Valley										La Cocha Lake		
Sample	JC001	JC002	JC003A	JC003B	JC004	JC007	JC009	JC010	JC011	JC012	JC014A	JC015	JC016
wt. %													
SiO2	75.0	71.5	58.3	46.1	64.1	62.1	58.2	48.0	65.5	43.3	56.4	73.6	69.5
TiO2	0.3	0.5	0.7	2.8	0.6	0.7	0.8	1.0	0.5	1.4	0.9	0.2	0.2
Al2O3	13.4	13.7	18.5	15.1	14.7	16.2	17.0	16.2	16.7	12.1	16.6	14.0	15.8
Fe2O3	3.0	4.7	6.4	14.8	6.0	6.7	7.4	9.4	4.7	10.6	8.0	2.1	2.8
MgO	0.7	1.1	2.8	5.2	3.1	2.7	3.1	6.3	1.7	11.9	3.7	0.5	1.0
CaO	1.4	2.4	6.1	6.4	5.5	4.8	6.2	8.4	4.2	9.9	7.5	1.6	2.7
Na2O	4.5	4.0	4.2	3.2	3.1	3.3	3.2	2.7	3.4	2.6	3.4	4.2	5.1
K2O	0.9	1.2	2.9	3.2	1.7	1.7	3.0	1.3	3.4	1.1	1.1	1.9	1.6
P2O5	0.1	0.1	0.3	1.2	0.2	0.2	0.3	0.3	0.2	0.8	0.3	0.1	0.2
MnO	0.1	0.2	0.2	0.5	0.1	0.1	0.1	0.2	0.1	0.2	0.2	0.0	0.1
Cr2O3	<0.002	0.0	0.0	0.0	0.0	0.0	0.0	0.0	0.0	0.1	0.0	<0.002	<0.002
SrO	0.0	0.0	0.1	0.0	0.0	0.1	0.1	0.1	0.1	0.1	0.1	0.0	0.1
BaO	0.0	0.1	0.1	0.1	0.1	0.1	0.1	0.1	0.2	0.1	0.1	0.1	0.1
LOI	1.5	1.8	1.0	0.6	1.2	1.3	1.2	5.4	1.1	2.8	2.0	1.4	1.6
TOTAL	100.9	101.1	101.5	99.1	100.3	100.0	100.7	99.3	101.6	96.8	100.1	99.8	100.5
ppm													
Li	<10	10.0	20.0	30.0	10.0	40.0	10.0	20.0	10.0	20.0	10.0	<10	10.0
Cr	10.0	30.0	50.0	20.0	20.0	10.0	30.0	150.0	20.0	650.0	40.0	10.0	10.0
Co	5.0	6.0	17.0	16.0	17.0	10.0	18.0	27.0	9.0	43.0	17.0	4.0	5.0
Ni	1.0	<1	13.0	5.0	11.0	<1	9.0	55.0	5.0	306.0	10.0	<1	3.0
Cu	41.0	47.0	13.0	17.0	52.0	6.0	58.0	30.0	12.0	29.0	44.0	7.0	16.0
Zn	175.0	204.0	229.0	512.0	67.0	100.0	82.0	114.0	55.0	107.0	73.0	29.0	22.0
Ga	20.6	21.6	24.8	24.6	18.0	18.9	22.2	19.9	19.1	20.3	20.4	15.9	15.2
As	11.0	23.0	<5	<5	<5	<5	<5	<5	<5	<5	<5	<5	<5
Rb	28.8	40.6	98.8	84.5	52.8	43.3	87.8	35.0	93.4	21.9	28.1	46.9	38.3
Sr	129.0	120.0	526.0	177.0	396.0	496.0	590.0	781.0	551.0	923.0	667.0	350.0	504.0

Ag	<0.5	<0.5	<0.5	<0.5	<0.5	<0.5	<0.5	<0.5	<0.5	<0.5	<0.5	<0.5	<0.5
Cd	4.0	3.8	0.5	0.6	<0.5	<0.5	<0.5	<0.5	<0.5	<0.5	<0.5	<0.5	<0.5
Sn	1.0	2.0	3.0	1.0	1.0	1.0	2.0	1.0	1.0	1.0	1.0	1.0	1.0
Cs	0.3	0.7	2.2	2.3	1.1	8.5	2.1	1.4	2.1	0.4	0.8	1.0	0.7
Ba	394.0	538.0	1060.0	1325.0	563.0	595.0	1010.0	771.0	1750.0	704.0	439.0	932.0	856.0
Tl	<10	<10	<10	10.0	<10	<10	<10	10.0	<10	<10	10.0	<10	<10
Pb	168.0	83.0	30.0	31.0	7.0	5.0	12.0	5.0	13.0	3.0	5.0	<2	4
Th	2.7	4.4	9.5	1.0	5.7	1.1	5.2	2.6	7.3	16.1	2.6	5.9	2.9
U	1.1	1.9	2.0	0.4	1.1	0.5	1.6	0.6	2.0	3.2	0.9	1.4	0.7
Nb	9.8	14.6	12.6	8.5	7.3	4.3	9.3	4.6	6.1	21.4	5.2	5.0	2.0
Zr	201.0	337.0	266.0	136.0	55.0	86.0	253.0	105.0	214.0	186.0	126.0	135.0	157.0
V	16.0	19.0	140.0	344.0	174.0	107.0	170.0	224.0	82.0	258.0	202.0	26.0	54.0
Hf	5.2	8.5	6.2	3.4	1.7	2.3	6.1	2.6	5.5	4.3	3.4	3.4	3.5
Mo	2.0	2.0	1.0	2.0	1.0	8.0	2.0	2.0	<1	<1	2.0	<1	1.0
Ta	0.7	1.1	0.9	0.6	0.3	0.4	0.6	0.3	0.5	1.2	0.3	0.5	0.1
W	3.0	4.0	2.0	2.0	1.0	2.0	2.0	3.0	2.0	2.0	2.0	3.0	1.0
La	13.6	17.2	40.6	20.7	33.6	10.5	32.2	17.0	31.2	78.8	16.0	20.0	19.6
Ce	26.6	35.8	82.2	51.5	60.0	21.8	65.6	34.3	56.8	142.0	33.9	35.7	33.7
Pr	3.1	4.5	9.8	7.5	6.8	2.9	8.0	4.6	6.1	16.0	4.5	3.8	3.7
Nd	12.5	18.8	39.2	37.8	23.5	13.4	33.5	19.1	22.7	61.1	20.6	13.5	13.0
Sm	3.0	4.2	8.3	9.0	4.3	2.9	6.6	4.1	4.2	10.0	4.3	2.0	1.9
Eu	0.8	1.0	1.5	3.1	0.9	1.0	1.5	1.2	0.8	2.4	1.3	0.4	0.6
Gd	3.7	5.3	8.2	9.8	3.6	3.2	5.5	3.9	3.6	7.4	4.9	1.6	1.5
Tb	0.6	0.9	1.3	1.5	0.5	0.5	0.8	0.6	0.5	0.9	0.7	0.3	0.2
Dy	4.0	5.9	8.2	8.4	3.0	3.4	4.7	3.5	2.9	5.0	4.4	1.6	1.3
Ho	0.8	1.3	1.6	1.8	0.6	0.7	0.9	0.7	0.6	0.8	0.9	0.3	0.3
Er	2.8	4.4	4.9	4.8	1.9	2.0	2.5	1.8	1.7	1.9	2.5	0.9	0.8
Tm	0.4	0.7	0.7	0.6	0.3	0.3	0.4	0.2	0.3	0.3	0.3	0.2	0.1
Yb	2.8	4.5	4.6	3.7	1.8	2.1	2.4	1.9	1.8	1.7	2.6	1.1	0.9
Lu	0.5	0.7	0.7	0.6	0.3	0.3	0.4	0.3	0.3	0.2	0.4	0.2	0.2
Sc	7.0	14.0	15.0	36.0	20.0	12.0	20.0	25.0	9.0	22.0	26.0	3.0	6.0
Y	26.4	41.3	48.1	46.6	17.7	19.6	26.0	19.4	18.2	22.7	25.3	9.7	8.7

Table 2. Zircon U-Pb geochronology results.

Sample name	U (ppm)	Th/U	238U/206Pb	2σ absolute error	207Pb/206Pb	2σ absolute error	206Pb/238U Age	2σ absolute error	207Pb/206Pb	2σ absolute error	Preferred age	2σ absolute error (Ma)
Sibundoy Valley												
JC001												
CB2-JC01 - 2	870	0.9	35.6888	0.9	0.0508	0.0014	178.1	4.6	228	62	178.1	4.6
CB2-JC01 - 3	509.4	0.2	40.8664	1.1	0.0498	0.0017	155.8	4.2	181	79	155.8	4.2
CB2-JC01 - 4	851	0.6	35.3357	0.8	0.05095	0.0012	179.9	4	236	52	179.9	4
CB2-JC01 - 5	375	0.2	35.8038	0.6	0.0493	0.0014	177.6	2.8	179	66	177.6	2.8
CB2-JC01 - 7	569	0.1	36.1402	0.6	0.04955	0.0011	175.9	2.8	169	50	175.9	2.8
CB2-JC01 - 8	170.2	0.2	39.5726	0.9	0.0505	0.0024	160.9	3.5	210	110	160.9	3.5
CB2-JC01 - 14	915	0.2	35.8809	0.7	0.0507	0.0018	177.2	3.3	223	81	177.2	3.3
CB2-JC01 - 16	1175	1.5	36.9140	0.9	0.0542	0.003	172.3	4.3	360	130	172.3	4.3
CB2-JC01 - 24	773	0.3	36.8868	0.9	0.0505	0.0019	172.4	4	210	88	172.4	4
CB2-JC01 - 26	1474	3.2	36.0490	0.8	0.0498	0.0015	176.4	4	181	72	176.4	4
CB2-JC01 - 31	2198	0.3	35.3232	0.7	0.05109	0.00099	179.9	3.7	243	44	179.9	3.7
CB2-JC01 - 32	977	0.1	37.4672	0.6	0.04939	0.00097	169.8	2.8	163	46	169.8	2.8
CB2-JC01 - 34	2220	1.1	33.0033	1.4	0.0573	0.0033	192.1	8.4	560	130	192.1	8.4
CB2-JC01 - 38	729	0.3	35.0754	0.9	0.0506	0.0014	181.2	4.6	216	64	181.2	4.6
CB2-JC01 - 39	1770	1.0	33.9674	0.7	0.05248	0.0011	187	3.7	302	50	187	3.7
CB2-JC01 - 40	812	0.2	34.6861	0.6	0.04887	0.0011	183.2	3.2	138	52	183.2	3.2
CB2-JC01 - 41	1850	0.3	35.7526	0.7	0.0499	0.0012	177.8	3.5	184	57	177.8	3.5
CB2-JC01 - 45	2518	0.4	34.8918	0.9	0.0505	0.0014	182.2	4.4	214	59	182.2	4.4
CB2-JC01 - 47	1860	0.8	38.3877	1.1	0.0522	0.0023	165.8	4.9	287	100	165.8	4.9
CB2-JC01 - 51	830	0.2	36.2056	0.7	0.04942	0.0011	175.6	3.2	163	52	175.6	3.2
CB2-JC01 - 54	444	1.0	33.3556	0.8	0.0515	0.0028	190.4	4.6	250	130	190.4	4.6
CB2-JC01 - 56	3000	1.2	34.9040	0.9	0.05269	0.0012	182.1	4.6	313	51	182.1	4.6

CB2-JC01 - 57	2920	3.7	38.4025	1.4	0.0505	0.0012	165.7	5.9	213	55	165.7	5.9
CB2-JC01 - 58	1590	9.2	36.7242	0.9	0.0512	0.0014	173.2	4.1	241	63	173.2	4.1
CB2-JC01 - 60	5660	3.8	38.5208	1.5	0.0542	0.0028	165.2	6.3	370	110	165.2	6.3
CB2-JC01 - 61	1831	0.2	35.8423	0.7	0.0518	0.0017	177.4	3.6	269	74	177.4	3.6
CB2-JC01 - 67	2270	0.1	36.9140	0.6	0.04871	0.0011	172.3	2.9	130	50	172.3	2.9
CB2-JC01 - 68	584	0.2	37.2995	0.6	0.04935	0.001	170.5	2.9	160	47	170.5	2.9
CB2-JC01 - 70	365	0.3	35.1865	0.9	0.0497	0.0016	180.7	4.4	194	78	180.7	4.4
CB2-JC01 - 71	811	0.2	39.5726	0.7	0.0513	0.0014	160.9	2.8	249	64	160.9	2.8
CB2-JC01 - 72	1535	0.3	38.0518	1.0	0.0506	0.0013	167.2	4.4	217	58	167.2	4.4
CB2-JC01 - 73	697	0.2	38.3289	0.7	0.04945	0.0011	166	2.8	174	50	166	2.8
CB2-JC01 - 74	2204	0.2	37.4392	0.6	0.0497	0.00096	169.9	2.8	177	45	169.9	2.8
CB2-JC01 - 75	1010	0.3	36.0881	0.9	0.05055	0.0011	176.2	4.3	217	52	176.2	4.3
CB2-JC01 - 76	620	0.2	33.5796	0.7	0.0485	0.0018	189.2	3.8	119	84	189.2	3.8
CB2-JC01 - 78	198	0.2	36.6703	0.8	0.0494	0.0016	173.4	3.6	158	73	173.4	3.6
						JC003B						
CB2-JC03B - 1	580	0.3	36.1664	0.8502	0.0501	0.0021	175.8	4.1	195	93	175.8	4.1
CB2-JC03B - 2	343	0.4	40.4367	1.1446	0.0503	0.0022	157.5	4.4	202	100	157.5	4.4
CB2-JC03B - 3	180	0.6	32.8515	0.6044	0.0498	0.0017	193.3	3.5	188	81	193.3	3.5
CB2-JC03B - 4	577	0.4	36.7918	0.6091	0.0492	0.0016	172.9	2.8	150	74	172.9	2.8
CB2-JC03B - 5	800	0.4	40.5022	0.7710	0.04996	0.00091	157.2	2.9	189	42	157.2	2.9
CB2-JC03B - 6	1163	0.2	36.0231	0.9862	0.0493	0.0015	177.8	4.3	158	72	177.8	4.3
CB2-JC03B - 8	779	0.4	38.1388	0.8873	0.0529	0.0017	166.9	3.8	314	75	166.9	3.8
CB3-JC03B - 3	239.9	0.4	42.6076	1.4886	0.0526	0.002	149.6	5.1	300	90	149.6	5.1
CB3-JC03B - 4	333	0.4	38.5654	0.7734	0.0482	0.0017	165	3.3	105	77	165	3.3
CB3-JC03B -	1902	0.2	37.9363	0.6332	0.05049	0.0011	167.7	2.7	214	48	167.7	2.7

5												
CB3-JC03B - 6	2580	0.2	38.2117	0.8907	0.0526	0.0014	166.5	3.8	308	63	166.5	3.8
CB3-JC03B - 8	755	0.3	39.6511	0.6446	0.04931	0.00088	160.6	2.6	159	42	160.6	2.6
						La Cocha Lake						
						JC014A						
CB1-JC14A - 2	80.7	0.8	41.8936	0.7196	0.0481	0.0024	152.1	2.6	140	110	152.1	2.6
CB1-JC14A - 4	239.5	0.2	44.6828	0.9184	0.0494	0.0018	142.7	2.9	158	81	142.7	2.9
CB1-JC14A - 6	57.6	0.8	43.6300	1.2373	0.0502	0.0039	146.1	4.1	190	170	146.1	4.1
CB1-JC14A - 7	63.8	0.6	41.3736	1.2325	0.0513	0.0031	153.9	4.5	240	140	153.9	4.5
CB1-JC14A - 8	79.2	0.5	41.2882	0.6819	0.0509	0.003	154.3	2.5	220	140	154.3	2.5
CB1-JC14A - 9	42.5	0.8	41.0341	0.9766	0.0505	0.004	155.2	3.7	260	190	155.2	3.7
CB1-JC14A - 10	50.0	0.7	41.0846	0.8271	0.0513	0.0051	155	3.1	280	200	155	3.1
CB1-JC14A - 11	93.6	0.6	42.0875	0.8680	0.0488	0.0024	151.4	3.1	130	110	151.4	3.1
CB1-JC14A - 12	202.2	0.7	42.7716	0.8415	0.0488	0.0019	149	2.9	133	85	149	2.9
CB2-JC14A - 1	72.3	0.7	41.4938	1.0330	0.0513	0.0028	153.5	3.8	260	120	153.5	3.8
CB2-JC14A - 2	58.8	0.8	41.1015	0.6588	0.0477	0.0029	154.9	2.5	100	120	154.9	2.5
CB2-JC14A - 3	62.2	0.8	40.4367	0.8666	0.0494	0.0021	157.5	3.3	158	96	157.5	3.3
CB2-JC14A - 4	63.4	0.8	42.2297	0.7668	0.0502	0.0019	150.9	2.7	206	89	150.9	2.7
CB2-JC14A - 5	66.9	0.9	41.8936	0.7722	0.0511	0.0034	152.1	2.7	220	140	152.1	2.7
CB2-JC14A - 6	36.2	0.7	40.5351	0.9694	0.0495	0.0031	157.1	3.7	180	130	157.1	3.7
CB2-JC14A - 7	46.7	0.5	40.3877	0.8156	0.0486	0.003	157.7	3.2	110	130	157.7	3.2

CB2-JC14A - 8	79.0	0.7	41.0678	0.8095	0.0502	0.0026	155.1	3	240	110	155.1	3
CB2-JC14A - 9	70.9	0.7	42.2297	0.8738	0.0496	0.0033	150.9	3.1	160	140	150.9	3.1
CB2-JC14A - 10	50.3	0.7	41.7188	0.9050	0.0498	0.0027	152.7	3.3	170	120	152.7	3.3
CB2-JC14A - 11	46.1	0.7	41.5282	0.8795	0.0498	0.0028	153.4	3.2	180	120	153.4	3.2
CB2-JC14A - 12	42.3	0.6	40.8163	0.9163	0.0492	0.0031	156	3.5	180	130	156	3.5
CB2-JC14A - 15	101.9	0.7	42.6985	0.8751	0.05	0.0022	149.2	3	185	98	149.2	3
CB2-JC14A - 16	53.5	0.5	41.4250	0.8237	0.0485	0.0021	153.8	3	120	97	153.8	3
CB2-JC14A - 21	77.5	0.7	40.4531	0.7691	0.0521	0.0029	157.4	3	290	130	157.4	3
CB2-JC14A - 22	91.1	0.8	42.1941	1.0504	0.0497	0.0029	151	3.7	200	140	151	3.7
CB2-JC14A - 23	232.0	1.0	42.2119	0.7662	0.0505	0.0022	150.9	2.7	210	100	150.9	2.7
CB2-JC14A - 24	369.0	0.3	47.7555	1.2771	0.0509	0.0026	133.6	3.5	220	110	133.6	3.5

Sample name	U (ppm)	Th/U	238U/206Pb	1σ% error	207Pb/206Pb	1σ% error	206Pb/238U Age	1σ absolute error	207Pb/206Pb	1σ absolute error	Preferred age	1σ absolute error (Ma)
						JC016						
JC016_2	542	1.4	41.21	0.73	0.0507	0.0014	154.3	2.7	225.2	31.9	154.3	2.7
JC016_4	1359	1.6	41.63	0.57	0.0492	0.0007	153.0	2.1	157.8	17.0	153.0	2.1
JC016_5	521	1.2	40.81	0.74	0.0505	0.0014	155.8	2.8	217.2	30.8	155.8	2.8
JC016_7	978	1.3	41.44	0.56	0.0496	0.0010	153.6	2.1	178.6	23.2	153.6	2.1
JC016_8	815	1.4	41.94	0.61	0.0499	0.0011	151.7	2.2	188.8	26.1	151.7	2.2
JC016_9	986	1.8	42.17	0.60	0.0490	0.0009	151.1	2.1	147.4	21.3	151.1	2.1
JC016_10	1007	2.0	41.75	0.65	0.0508	0.0010	152.3	2.4	232.1	21.7	152.3	2.4
JC016_12	529	1.5	42.36	0.77	0.0507	0.0013	150.1	2.7	227.0	29.1	150.1	2.7

JC016_13	1115	2.0	41.83	0.53	0.0504	0.0010	152.1	1.9	211.9	22.1	152.1	1.9
JC016_15	342	1.3	42.32	0.92	0.0516	0.0016	150.0	3.2	269.8	34.2	150.0	3.2
JC016_16	720	1.5	43.26	0.76	0.0531	0.0011	146.5	2.6	333.2	24.0	146.5	2.6
JC016_17	667	1.3	42.41	0.72	0.0491	0.0010	150.2	2.5	152.6	23.1	150.2	2.5
JC016_18	535	1.8	41.91	0.71	0.0533	0.0013	151.2	2.5	339.7	27.6	151.2	2.5
JC016_19	633	1.2	40.86	0.64	0.0510	0.0013	155.5	2.4	239.6	29.2	155.5	2.4
JC016_20	452	1.5	42.03	0.68	0.0516	0.0016	151.1	2.4	268.1	34.4	151.1	2.4
JC016_21	562	1.2	43.12	0.72	0.0508	0.0014	147.5	2.5	230.6	30.9	147.5	2.5
JC016_22	304	1.3	41.79	0.77	0.0508	0.0020	152.1	2.8	231.9	44.2	152.1	2.8
JC016_23	784	1.6	41.28	0.54	0.0525	0.0014	153.7	2.0	308.2	30.7	153.7	2.0
JC016_27	559	1.5	42.09	0.72	0.0482	0.0015	151.6	2.6	107.3	36.7	151.6	2.6
JC016_28	784	1.2	41.20	0.67	0.0490	0.0011	154.6	2.5	146.2	26.5	154.6	2.5
JC016_29	478	1.1	42.60	0.73	0.0511	0.0014	149.2	2.6	244.5	31.8	149.2	2.6
JC016_30	599	1.7	42.44	0.64	0.0488	0.0014	150.2	2.3	137.1	33.3	150.2	2.3
JC016_31	702	1.6	41.48	0.58	0.0485	0.0012	153.7	2.1	123.1	28.0	153.7	2.1
JC016_32	789	1.4	42.45	0.60	0.0499	0.0011	149.9	2.1	190.9	25.4	149.9	2.1
JC016_33	510	1.3	41.03	0.63	0.0503	0.0016	155.0	2.4	210.0	36.2	155.0	2.4
JC016_34	1079	2.1	42.22	0.68	0.0508	0.0010	150.6	2.4	231.6	22.4	150.6	2.4
JC016_35	1307	1.7	41.32	0.57	0.0508	0.0008	153.8	2.1	233.9	17.7	153.8	2.1
JC016_36	1095	1.4	42.26	0.54	0.0529	0.0011	150.0	1.9	326.6	22.6	150.0	1.9
JC016_38	991	2.3	39.96	0.78	0.0522	0.0010	158.7	3.1	295.8	22.5	158.7	3.1
JC016_40	1487	1.5	41.13	0.54	0.0495	0.0008	154.8	2.0	170.2	19.6	154.8	2.0
JC016_41	1221	1.4	41.56	0.58	0.0492	0.0007	153.3	2.1	156.8	17.5	153.3	2.1
JC016_42	461	1.4	42.21	0.90	0.0501	0.0016	150.7	3.2	198.4	35.9	150.7	3.2
JC016_45	683	1.8	41.85	0.73	0.0496	0.0011	152.1	2.6	178.4	26.4	152.1	2.6
JC016_46	943	1.2	41.37	0.54	0.0499	0.0010	153.8	2.0	189.8	23.0	153.8	2.0
JC016_47	697	1.6	41.29	0.58	0.0511	0.0008	153.9	2.2	246.2	18.7	153.9	2.2
JC016_48	463	1.7	40.43	0.68	0.0533	0.0015	156.7	2.6	339.8	31.2	156.7	2.6
JC016_49	628	1.4	41.89	0.54	0.0498	0.0012	151.9	2.0	187.3	28.6	151.9	2.0

JC016_50	1414	1.4	41.90	0.51	0.0499	0.0008	151.9	1.8	190.7	18.8	151.9	1.8
JC016_51	898	1.7	41.94	0.67	0.0505	0.0008	151.6	2.4	216.2	19.3	151.6	2.4